Science of the Total Environment 933 (2024) 172398

Contents lists available at ScienceDirect

Science of the Total Environment

journal homepage: www.elsevier.com/locate/scitotenv

A multisensor approach coupled with multivariate statistics and geostatistics for assessing the status of land degradation: The case of soils contaminated in a former outdoor shooting range

S. Vingiani [a], G. Buttafuoco [b], M. Fagnano [a], A. Guarino [c], C. Perreca [a,*], S. Albanese [c]

[a] Department of Agricultural Sciences, University of Naples Federico II, Portici, NA, Italy
[b] National Research Council of Italy, Institute for Agriculture and Forestry Systems in the Mediterranean, Rende, CS, Italy
[c] Department of Earth, Environmental and Resources Sciences, University of Naples Federico II, Naples, Italy

HIGHLIGHTS

- EMI data allows reproducing soil contamination pattern due to the shooting activity.
- ECa was used as an external drift in kriging to improve PTEs prediction.
- Highly compacted soil layers occurred in the areas mostly contaminated by PTEs.
- Robust PCA disclosed the relations between proximal sensing data and PTEs.
- PC1 might explain the anthropic effects produced by the shooting activities.

GRAPHICAL ABSTRACT

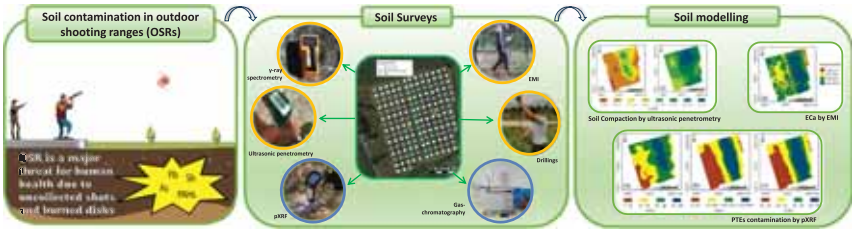

ARTICLE INFO

Editor: Damià Barceló

Keywords:
Electro-magnetic induction (EMI)
Potentially toxic elements (PTE)
Compositional data
γ-ray spectrometry
pXRF
Ultrasonic penetrometry
South Italy

ABSTRACT

Soil contamination in outdoor shooting ranges (OSRs) is a major threat for human health, particularly when, after the end of activities, the land is used for recreational areas or agricultural production. The status of land degradation of an OSR in southern Italy was assessed using a multisensor approach. It was based on: i) proximal sensors, including electromagnetic induction (EMI) for measuring soil electrical conductivity (ECa) and magnetic susceptibility (MSa), γ-ray spectrometry for K, eU and eTh analyses and ultrasonic penetrometry detecting cone index (CI) data representative of soil's strength, ii) field surveys on soil thickness (ST), and iii) laboratory analyses of potentially-toxic-elements (PTEs) by portable X-ray fluorescence spectrometry and polycyclic aromatic hydrocarbons (PAHs) by gas-chromatography. Spatial variability of measurements was modelled and mapped using geostatistical methods. The most densely measured covariate (i.e., the ECa of the topsoil) was used within kriging with external drift to improve the PTEs predictions. The PTEs maps were complemented by maps of spatial uncertainty. A robust multivariate principal component analysis (rPCA) was applied to proximal sensor and laboratory data and allowed to identify associations of PAHs, lead, CI with the topsoil ECa along the first component (PC1), highlighting the correlation between land anthropogenic effects and EMI measures; while the association between the ST (estimating the depth of underground travertine hard-layers) and the bottom soil ECa and MSa along the second component (PC2) evidenced the influence of soil stratigraphy on the EMI measures. This study demonstrates that the simultaneous use of different proximal sensors associated with laboratory analysis can allow to assess and model the spatial variability of the land degradation status of an OSR, including

* Corresponding author.
E-mail address: carlo.perreca@unina.it (C. Perreca).

https://doi.org/10.1016/j.scitotenv.2024.172398
Received 5 February 2024; Received in revised form 3 April 2024; Accepted 9 April 2024
Available online 25 April 2024

soil compaction, organic and inorganic contamination. The correlation between EMI data with the PTEs content highlights the potential of this technique in the field of soil contamination.

1. Introduction

Outdoor shooting ranges (OSRs) represent a recreational facility gathering the interest of several millions of people in the world, mostly in USA, Canada, Sweden, and Finland. As reported by the Italian National Olympic Committee (CONI) in the 2008, the number of Italian members registered with the International Practical Shooting Confederation (IPSC) highly increased (+38.6 %) during the 1997–2007 decade (CENSIS Servizi, 2008) and remained stable at approximately 20 thousand registered people to date, even if during COVID-19 pandemic the number of people involved in this sport had a decline similar to other recreational activities (CONI, 2023). Environmental concerns relating to the presence of expended and uncollected lead bullets and shooting targets in the soil of OSRs are documented for several countries (Cao et al., 2003; Chen et al., 2002; Johnson et al., 2005; Laporte-Saumure et al., 2011; US EPA, 2001). In these areas, long operating times, often extending to several decades, produced soil contamination due to inadequate environmental protection measures. Potentially toxic elements (PTE), including lead (Pb), antimony (Sb), copper (Cu), zinc (Zn), arsenic (As), nickel (Ni), and organic compounds, such as polycyclic aromatic hydrocarbons (PAHs), are often found in most OSRs soil (Basunia and Landsberger, 2001; Clausen and Korte, 2009; ITRC (Interstate Technology and Regulatory Council Small Arms Firing Range Team), 2003; Scheetz and Rimstidt, 2009; U.S. Army Corps of Engineers Fort Worth District, 2014). Lead (up to 93.1 % of the whole mass), followed by Sb (ranging from 2.8 to 3.1 %), As (ranging from 0.2 to 0.2 %), Bi (<0.03 %) and Cu (<0.01 %), respectively, are the main constituents of a bullet (ARPAV - Agenzia Regionale per la Prevenzione e Protezione Ambientale del Veneto, 2014; Johnson et al., 2005; Laporte-Saumure et al., 2011; Randich et al., 2002). Therefore, in a shooting range soil, Pb and Sb, especially, are expected to largely exceed the natural soil concentrations (Agency for Toxic Substances and Disease Registry, 1992; Caporale et al., 2018a; Filella et al., 2002; Noll, 2003; Rooney et al., 1999), and can be considered long-term persistent and dangerous contaminants due to their low mobility (Gisbert et al., 2003; Knox, 2000; Singh and Gräfe, 2010). Weathering processes affecting bullet fragments cause Pb and Sb releases into the soil solution, posing an environmental hazard due to their toxicity for the biota (Rooney et al., 1999; US EPA, 1979). Hazards can also indirectly involve human health when sensitive areas (such as agricultural lands) are in the vicinity of an operating or decommissioned shooting range. In facts, contaminated dust raised from an OSR and blown by the wind to its surroundings can settle in agricultural fields and become part of the trophic chain following absorption by roots and leaves of plants and vegetables. This holds true also if, in case of a dismissed OSR, the land use of the area, previously occupied by the facility, changes for an agricultural use or if the site will be intended for residential or public green use. Indeed, it is reported that soil Pb could be accumulated in plants (Muhammad et al., 2019) and can enter the food chain, or transported as dust, inhaled, or ingested by humans and animals (Ishtiaq et al., 2018; Saddique et al., 2018). Children (1–16 years) among the human population are the most vulnerable to Pb poisoning and can suffer mental impairment and memory loss (Alloway, 2013). Variety and intensity of contamination changes among different OSRs depending on the type of shooting, management practices, operating time, frequency and number of visits, and environmental characteristics of the site. Soil contamination is likely to be non-uniform and its distribution depends on the structure of the OSRs and factors not easily determinable. Moreover, spatial variability of contamination within the same OSRs can also occur since of the shooting ballistics and can be associated with other soil degradation processes (including soil compaction due to plant management), poorly or not investigated in these lands. Indeed, assuming that an operating OSR is normally crossed by heavy vehicles for maintenance and weeding purposes, soil compaction could occur bringing to low conductivity and the development of near-surface stagnant water phases with the onset of anaerobic conditions potentially affecting soil biogeochemistry. Therefore, modelling the spatial distribution of soil contamination can be complemented and improved by other physical characteristics. This would fill our lack of knowledge on the exact determinism of the soil contamination process and allow for better precision in relation to expected remedial actions in the investigated area.

Soil sampling is necessarily limited to a few locations and provides only a fragmentary picture of the soil contamination. No matter how accurate methods of modelling and mapping soil contaminants may be used, none of them are free from generating spatial uncertainty at unsampled locations. A major contribution to the modelling and mapping of soil processes, in addition to contamination, has come from many manufacturers; they have proposed new technologies with different advantages and disadvantages, accuracy, and costs. These technologies include different sensors and sensing modalities, from proximal or remote in relation to the distance (less or >2 m) of the sensor to the soil surface to invasive or non-invasive (if the sensor is inside or outside the measurement volume); they can also be active or passive if the system includes or not an external energy source; mobile or stationary depending on whether the system is capable of measuring in motion or only in stationary mode (McBratney et al., 2011). Geophysical methods as automatic resistivity profiling (ARP), electromagnetic induction (EMI) (Corwin, 2005; Daniels et al., 2008b; Doolittle and Brevik, 2014), ground penetrating radar (GPR) (Daniels et al., 2008a), spectrometric (γ-ray, X-ray fluorescence-XRF) (César de Mello et al., 2021; Gozukara et al., 2022; Van Der Klooster et al., 2011a), visible (Vis-NIR), medium (MIR) and near infrared (NIR) spectroscopy (Conforti et al., 2018; Gozukara et al., 2022; Lagacherie and Gomez, 2018; Van Groenigen et al., 2003) are among these. They have extensively been used in the various fields of application of soil science (e.g., precision agriculture, soil remediation, etc.) (Ben-Dor et al., 2008, 2009, 2013; Buttafuoco et al., 2019, 2021; Castrignanò et al., 2019; Chabrillat et al., 2019; De Benedetto et al., 2012; Doolittle and Brevik, 2014a; Stevens et al., 2008; Van Der Klooster et al., 2011a) and the spatial accuracy of data has extremely improved since acquired data are georeferenced with the field support of the global navigation satellite system (GNSS) receivers. Geophysical techniques are strongly sensitive to several physical soil properties, including clay and moisture content, bulk density (Altdorff et al., 2016; McBratney et al., 2005; Priori et al., 2014; Van Der Klooster et al., 2011b; Viscarra Rossel et al., 2007; Walter et al., 2015), organic matter, as well as soil chemical composition, including salinity (Bouksila et al., 2012; Corwin and Lesch, 2005a; Paz et al., 2020), pH (Huang et al., 2014), cation exchange capacity (CEC) (Triantafilis et al., 2009) and elemental concentration (Kweon et al., 2013; Martínez et al., 2010; Martini et al., 2017; Molin and Faulin, 2013; Rhoades et al., 1990). Among the geophysical techniques, EMI is the most popular since the device does not require direct contact with the subsurface and can be towed behind a motorized vehicle (Corwin and Lesch, 2005a, 2005b; Doolittle and Brevik, 2014; Heil and Schmidhalter, 2017). As a matter of the fact, EMI can acquire very high volumes of data in the field allowing the coverage of wide portions of land surface in a reduced time at a low-cost. Although soil conductivity meters were designed to measure the soil electrical conductivity values (ECa), already for the first instruments (Tite and Mullins, 1969) was demonstrated that they responded also to soil magnetic properties, then magnetic susceptibility MSa, as recorded by EMI instruments, has been used to investigate artificial inclusions and structures in soil (Sadatcharam et al., 2020; Saey et al., 2016).

γ-ray spectrometry has been successfully applied during last decade as soil sensing technique to estimate mineralogical (Callegari et al., 2013; Martelet et al., 2013; Schuler et al., 2011) and compositional soil properties including clay, potassium, organic carbon and iron contents and soil pH (Viscarra Rossel et al., 2007; Wong et al., 2008, 2009; Wong and Harper, 1999). Measures can be carried out from either the ground or airborne platforms. Strengths and weaknesses of γ-ray spectrometry and EMI sensing techniques may complement each other when used in combination for soil mapping (Wong et al., 2008, 2010); it has been demonstrated (Taylor et al., 2010; Loonstra, 2011) that γ radiometry produced better predictions on near-surface soil layers than the EMI and vice versa.

Portable X-ray fluorescence (pXRF) analyser is another powerful proximal sensor for in situ or laboratory measures of total elemental composition in different materials (rock, soil, metal alloys, vegetables, etc.) (Ribeiro et al., 2017; Weindorf et al., 2014; Caporale et al., 2018b; Carr et al., 2008; Gholizadeh et al., 2015; Higueras et al., 2012; Horta et al., 2015; Hou et al., 2004; Wang et al., 2015; Zerboni et al., 2011) compared to conventional laboratory-based methods (Viscarra Rossel et al., 2011; Caporale et al., 2018a; Vingiani et al., 2022).

However, the combined use of different proximal sensors has improved some predictions of different soil properties (Andrade et al., 2022; Teixeira et al., 2022).

Nevertheless, for contaminated sites little known is the degree and spatial variability of land degradation effects in terms of soil compaction, because just in one recent study (Vingiani et al., 2022) measurements and maps of soil strength values have been provided despite their recognised impact on crop development. The penetrometer is among the most used instrument to assess soil compaction and strength in situ at several depths. Useful empirical negative correlations between soil penetration resistance and crop root growth (Bowen, 1976; Houben, 1974; Taylor, 1973; Taylor and Ratliff, 1969; Trouse, 1983; Voorhees, 1987), as well with the explorative capability of roots for water and nutrients (Barley et al., 1965; Busscher and Sojka, 1987; Gerard et al., 1982; Taylor et al., 1966) have often been obtained. Georeferenced spatial measurements by penetrometers can help identify areas affected by soil compaction faster and easier than standard bulk density, generally much applied to measure soil compaction (Stelluti et al., 1998).

The availability of different types of data does not solve problems unless they are used through appropriate methods that consider their nature.

Geostatistical methods (Matheron, 1971) are suitable and widely used in modelling the spatial structure of soil properties and processes, their interpretation and later mapping. These methods have been described in many texts (Chilès and Delfiner, 2012; Goovaerts, 1997; Olea, 1999; Wackernagel, 2003; Webster and Oliver, 2007) and are based on the correlation between pairs of sample values of a variable at different distance. These autocorrelations are distributed in space and exhibit a certain spatial structure (Matheron, 1963). This spatial dependence is modelled and enables the estimation of the variable at unsampled locations by using an interpolation technique, generically known as kriging, which provides the 'best', unbiased, linear estimate of a regionalized variable in an unsampled location, where 'best' is defined in a least-squares sense (Chilès and Delfiner, 2012; Matheron, 1971). However, although the kriging estimate is defined as 'best', it results in a smoothing of the distribution of estimates that, in the case of soil properties with highly skewed distributions such as PTE, the maps produced may not be representative of the true variability (Leuangthong et al., 2004). If the reproduction of spatial features is more important than local accuracy, stochastic simulation, which was developed to provide a measure of spatial uncertainty, is much more useful than traditional interpolation algorithms in reproducing the full spectrum of the spatial variability of data and can provide a single improved 'estimated' map (Deutsch and Journel, 1997).

Geochemical concentrations in soils are compositional in nature because they are parts of some whole and single parts carry only relative information (Pawlowsky-Glahn et al., 2015). The statistical analysis of such data sets is based on the Aitchison (1986)'s idea and its developments that if all chemical elements in a soil sample are analysed, their concentrations sum up to a constant (Pawlowsky-Glahn et al., 2015; Pawlowsky-Glahn and Buccianti, 2011). Therefore, the relationships that variables have to one another are conditioned and no single chemical element is free to vary independently from the rest of the elements included in the composition. Other problems can occur and standard statistical techniques for unconstrained random variables cannot be used to analyse compositional data in the raw (Aitchison, 1986; Pawlowsky-Glahn et al., 2015; Pawlowsky-Glahn and Buccianti, 2011).

The study presented here was carried out in southern Italy within a land declared unsuitable for agricultural and forest-pastoral production by the Italian Ministry of Agricultural, Food and Forestry Policies, due to a documented contamination of Pb, Sb, PAHs, dioxins, polychlorinated biphenyls (PCBs) and C > 12 hydrocarbons; soil contamination was associated with an extensive long term (approximately 10 years of activity) use of the site as an outdoor shooting range (OSR). In this context, the main objective was assessing the status of degradation, by applying an approach based on multisensor surveys (electromagnetic induction, gamma-ray spectrometry, ultrasonic penetrometry), including different field and laboratory measurements. The approach provided a modelling of the spatial patterns of different proximal sensors (EMI, γ-ray, and penetrometry) data and their spatial relations with the concentrations of some contaminants (PTEs and PAHs) exceeding the regulatory thresholds. A geostatistical approach was used for modelling spatial patterns of contaminants, proximal sensors data and their relationships. The latter to define possible covariates more densely measured than contaminants and for improving their estimates at unsampled locations. Moreover, modelling of EMI measurements (such as ECa and MSa data) was carried out to obtain insights on different soil volumes and direct measures of soil thickness for inferring soil stratigraphy, layers occurrence, and their potential role on mobility of contaminants. Finally, a multivariate approach based on robust principal component analysis (rPCA) was used to define groups of associate variables and obtain insights about anthropogenic processes or environmental conditions.

2. Materials and methods

2.1. Study area

The area is in Campania region (southern Italy), within the north-eastern sector of the municipality of Acerra. The historical use of the area (lat. 449,746 m E; long. 4,538,294 m N) has been reconstructed starting from the 90's thanks to the 1:10,000 Official Technical Cartography IGMI "Montefibre" (Provincia di Napoli, 1998) which labels it as "Tiro a piattello" (i.e., "Skeet shooting"). The presence of the facility structures is still evident after more than two decades in a satellite image of May 2022 retrieved from the Google Earth service (Fig. 1). Images also allow to clearly identify the presence of two main rectangular zones (both NW-SE oriented) which are physically separated by a small longitudinal bank (named "arginello"). The shooting positions were in the western part of the site and the shot trajectory was SW-NE.

Evidence of agricultural use (including traces of tillage and vegetation growth) of the site are provided by the Google Earth images starting from December 2012. Agriculture was carried out on the site until March 2015 when agricultural and forestry-pastoral production was forbidden because of the high concentrations of PTEs (Pb, Sb) and organic compounds (dioxins, PAHs, C > 12 hydrocarbons, PCBs) found in soil and confirmed by the regional environmental protection agency (ARPAC). At the time of the field surveys the site was uncultivated and remains so today. In the surroundings, agricultural use of the lands is practiced. Urban or industrial areas are outside of approximately 2 km of radius around the study site. The official prescription from the MIPAAF

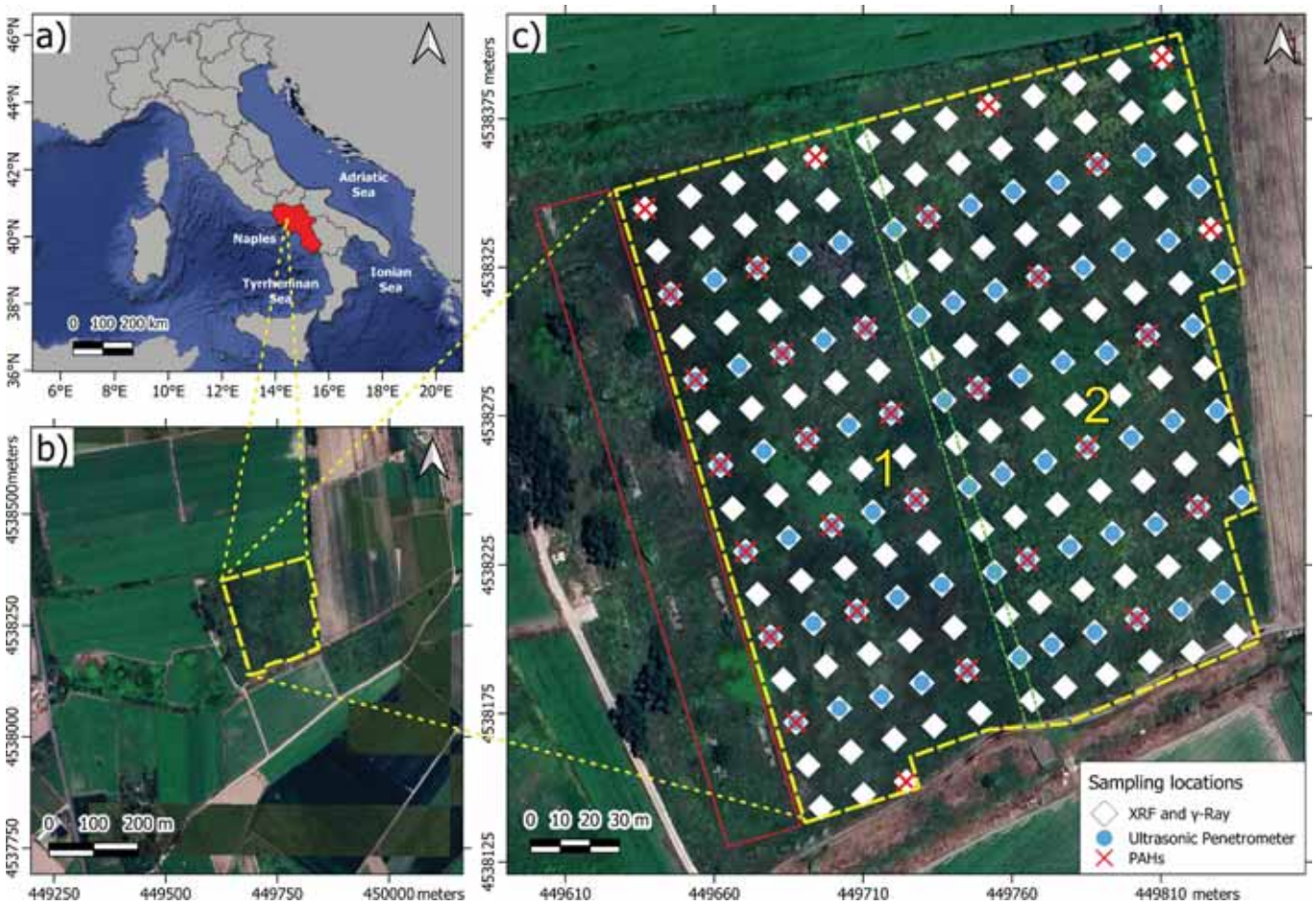

Fig. 1. Location of the study site from the country to the field scale. On the right, the surveyed field reporting soil sampling locations. The dotted yellow line delimits the investigated area, made by the zone 1, the closest to the shooting positions (delimited by the solid red line), and the zone 2; the dotted green line delimits the «arginello», a small longitudinal anthropogenic bank.

(Ministry of Agricultural, Food and Forestry Policies) was to proceed with the characterization of the site to assess the risk and possibly proceed with the remediation.

From the geological point of view, the study area is in the central-eastern sector of the Piana Campana Plain, which is a structural depression elongated in the NW-SE direction, filled by Plio-Quaternary sedimentary and volcanic deposits produced by the main eruptive centres (Phlegrean Fields, Somma-Vesuvius complex, Roccamonfina) of the plain (Putignano et al., 2012). The Geological map (Foglio 172 – Napoli, 1:100.000 scale) (I.G.M. Istituto Geografico Militare, 1967) reports the presence in the area of a swamp zone filled by volcanoclastic silty deposits intercalated by a spongic calcareous layer (vacuolar travertine layer) at shallow depth. The travertine layer probably originated by the degassing of carbonated groundwater proceeding from some mineral springs close to the foothills of the Apennine Chain at the border of the Campania Plain.

The area is covered by two pedological units (Di Gennaro and Terribile, 1999), one is in the site northern part belonging to the Regi Lagni alluvial plain, mantling travertine shallow layers where soils are classified as Pachi-Vitric Andosols (Calcaric, Gleyic) (IUSS Working Group WRB, 2014) and Vitrandic Haplustolls fine silty, mixed, thermic (Soil Survey Staff - NRCS/USDA, 2014). Andosols and andic-like (vitric soils) soils are widely spread over the Campania region (Vingiani et al., 2018) and extensively used for agriculture. The other unit is in the southern part of the field and includes soils developed on the foothill distal plain of the Mts of Cancello by Phlegrean and Vesuvius pyroclastic deposits mantling the shallow travertine layer and were classified as Vitri-Leptic Calcisols (IUSS Working Group WRB, 2014) and Lithic Petrocalcic Calciustepts ashy, glassy, thermic (Soil Survey Staff - NRCS/USDA, 2014).

The climate is warm temperate typical of southern Italy with dry and hot summer. Precipitations occur mainly in autumn and winter with a long-term (1991–2021) average annual precipitation of 1214 mm. The least rainy month is July with an average monthly precipitation of about 27 mm, whereas the rainiest month is November with an average monthly precipitation of about 182 mm. The long-term (1991–2021) average annual temperature is 15.4 °C with a minimum average annual value in January (7 °C) and a maximum one in August (30.2 °C) (Climate Acerra by Climate-Data.org, 2024).

2.2. Soil sampling

Soil samples in the shooting area (SA) were collected at the nodes of a regular grid (15 m × 15 m) at two depths (0–15 cm and 15–30 cm) and sample locations (a total of 174) were georeferenced by means of an external GSSI (±4 m) equipment (Fig. 1c). Additional soil samples were collected at 15 locations assumed to be uncontaminated (to be used as control samples, CS) in agricultural fields in the proximity of the shooting range (within 50 m from the contaminated area). The assumption of no contamination was then verified by laboratory determination of the PTEs concentrations under study.

At each location and for each depth of interest, the soils were sampled by stainless steel hand auger in triplicate, mixed and the composite sample was put in a plastic bag. Approximately 500 g of soil was collected for each sample and the total samples were 348 in SA and

30 in the CS. The applied procedure agreed with the IAEA guidelines (IAEA (International Atomic Energy Agency), 2004).

For the polycyclic aromatic hydrocarbons (PAHs) analysis, only 30 sampling locations were selected at the nodes of the above grid. At each location, the vegetated cover was removed for a total area of ~1 m^2, and a representative amount of soil (approximately 1 kg) was collected in a depth interval between 0 and 20 cm below the surface. Soil samples were put in glass jars with airtight screw caps and stored in dark conditions at 4 ± 2 °C during the transport to the laboratory.

Finally, a private company (i.e., Trivel Sondaggi SpA) was engaged to perform 20 core drillings from the surface down to 100 cm of depth and holes for 3 piezometers installation until 12–15 m of depth, applying a CMV MK 400 rotation probe. The spatial distribution of the sampling points was decided according to preliminary EMI surveys and their distance is around 40–60 m.

2.3. Proximal soil sensors analysis

2.3.1. Electromagnetic induction (EMI) survey

Apparent electrical conductivity (ECa) data were collected using a CMD Mini-Explorer device (GF Instruments, Brno, Czech Republic). The CMD electromagnetic (EM) conductivity meters enable fast contactless mapping of soil electrical conductivity (ECa) and in-phase (MSa), at both shallow and wide depths. The CMD Mini-Explorer was used to measure ECa in vertical coplanar (VCP) and horizontal coplanar (HCP) modes. VCP and HCP dipole configurations were obtained by rotating the probe 90° axially. The probe operates at 30 kHz frequency and three receiver coils are arranged along the probe, following 0.32 (ρ32), 0.71 (ρ71) and 1.18 (ρ118) m distances from the transmitter coil. The instrument has an effective depth investigation range of 0.5, 1.0, and 1.8 m in the HCP mode, and 0.25, 0.5, and 0.9 m by using the VCP configuration. Surveys were conducted along parallel transects keeping a spacing of 15 m in between and 8148 measures were acquired in VCP mode, while 7729 in HCP.

Soil conductivity meters respond also to soil magnetic properties. This effect occurs when the primary field intercepts magnetic materials and the secondary field is produced by the magnetic susceptibility of the features. The received secondary field wave is regarded as 'in-phase' with the primary field, then in-phase is defined as relative quantity in ppt (part per thousand) of primary magnetic field and is closely related to magnetic susceptibility (MSa) of measured material. The in-phase is especially used to detect artificial metal objects, including cables, pipes, reinforced concrete, tanks etc., in soil. However, in-phase measurements are sensitive to ferromagnetic minerals in soil, such as magnetite, pyrrhotine, maghemite, cassiterite, native iron, chromite. Effective depths investigation ranges are the same of ECa. Both ECa and MSa measures were acquired in continuous by hand transport of the instrument, which was kept at around 20 cm from the ground, and georeferenced by internal GSSI.

2.3.2. γ-ray spectrometry measurements

Spectrometric γ-ray survey was carried out in static mode and the radioactivity was measured at the same 174 locations of the regular grid used for the soil sampling. The equipment used was a Gamma Surveyor GF Instrument which is a γ-ray spectrometer designed to measure natural and artificial radioisotopes in the ground. The instrument factory calibration ('Factory") was set to high-volume uranium standard and the geometrical factor G = 1 - h/r (h is the height of the middle of the detector above the pad and r the diameter of the pad). Total energy window was set from 0.12 to 3.00 MeV. Minimization of local relief variation causing effects on radioelement distribution was obtained placing the detector directly on the earth surface. The "Spectrum and Assay" mode was selected in the device menu and, for the stabilization of the automatic gain control, measure time of 300 s was taken at each station. A reference isotopic source of Cs-137, with an approximate activity of 15 kBq, was used to automatically control the system gain and avoid any possible shift caused by temperature effect or component ageing. Determinations of eU and eTh were based on measured γ -radiation from the decay of ^{214}Bi (1.76 MeV) in the ^{238}U decay series and from ^{208}Tl (2.62 MeV) in the ^{232}Th series. The primary decay of ^{40}K (1.46 MeV) was measured directly. Concentration of K, eU and eTh was determined investigating three energy windows by recording γ-rays associated with characteristic peaks in the decay spectra of ^{40}K, ^{238}U and ^{232}Th. The total count energy window was set using the range from 0.12 to 3.00 MeV. Total elemental concentrations were reported in % for K, in mg/kg for eTh and eU, in while the nGy h^{-1} units were used to report the Dose Rate. For the selected counting time of 300 s, the detection limit is estimated to be 0.03 % for K, 0.2 mg/kg for eU and 0.3 mg/kg for eTh (Chiozzi et al., 2001). The survey was conducted in one day (on July 15th 2019), in absence of any rainy event. Single measures (4 replicates) were performed on a yellow tuff block used as reference standard material.

2.3.3. Penetrometry surveys

Complementary surveys were applied in field to assess the spatial variability of soil compaction and soil thickness (ST) until hard-lithic layers by ultrasonic cone penetrometer (until 60 cm of depth) and stainless-steel rod insert into the soil to a maximum depth of 2 m.

The ultrasonic penetrometer survey was based on the same grid used for the soil sampling, but at a smaller number of nodes (30 m × 15 m apart) and for a total of 73 locations. The ultrasonic cone penetrometer (Rimik CP20) was used for measuring and recording cone-index (CI) data representative of the soil's strength, typically recorded in kilo- (KPa) o mega-pascals (MPa)(Kees, 2005). The penetrometer was used for CI measurements of values up to 5 MPa and readings were made every 25 mm of depth increment up to a total depth of 60 cm from the surface.

Due to the technical limit to 60 cm of depth from the ground surface, the direct measure of the ST and the registration of the presence of hard layers within the soil range from 60 to 200 cm were done by a stainless-steel rod, equipped with handles and notches spaced 10 cm apart, which was carefully driven into the soil until meeting a compact layer. The ST by the steel rod was measured at all 174 nodes of the soil sampling grid (15 m × 15 m). The depth of the first hard (not penetrable) layer has been considered as the ST.

For both ultrasonic penetrometer and rod surveys, 4 replicates were carried out in a range of 0.5 m^2 for each point to avoid mistaken interpretation due to coarse fragments into the soil.

2.4. Laboratory analysis: pXRF and gas chromatography

The total element content of all the soil samples collected in the field (174 for each depth, 0–15 cm and 15–30 cm) was measured in laboratory by a Delta Professional (Olympus, DPO-4000) portable X-ray fluorescence analyser (pXRF). The soils were analysed in duplicate, after drying (at 30 °C) and sieving (< 2 mm). Scanning was performed with a Ta X-ray tube operating at 15–40 kV with integrated large area silicon drift detector (165 eV), using an 8 mm^2 window on smooth uniform surfaces completely in contact with the instrument to minimize surface effects. Two operational modes were used:

- "Soil", to quantify trace elements (including As, Cd, Cr, Cu, Fe, Mn, Nb, Ni, Pb, Rb, Sn, Sr, Th, Ti, U, V, Zn and Zr) by performing three beams of the same duration (30 s each) on each sample
- "Mining", to quantify the most concentrated elements (i.e. Al, Si, Ca, K), by performing two beams, for a total time a sample of 120 s.

Quality checks were performed on NIST 2710 A and 2711 A certified materials.

Finally, for the polycyclic aromatic hydrocarbons (PAHs) analysis, at the Merieux Nutrichiences Chelab S.r.l. laboratories in Volpiano (Italy) the soil samples were treated for detecting the levels of pyrene, benzo (a)

anthracene, chrysene, benzo (b) fluoranthene, benzo (k) fluoranthene, benzo (a) pyrene, dibenzo (a,e) pyrene, dibenzo (a,h) pyrene, dibenzo (a,i) pyrene, dibenzo (a,l) pyrene, indeno (1,2,3-cd) pyrene, dibenzo (a,h) anthracene, benzo (g,h,i) perylene. Specifically, samples were prepared for analysis in accordance with the U.S. EPA 3550C 2007 method, using an ultrasonic process to extract semi-volatile (SVOCs) and non-volatile (NVOCs) organic compounds from solid media. Each sample was mixed with anhydrous sodium sulphate to form a smooth flow powder to be extracted with solvent using ultrasonic extraction. The extracted compounds were subsequently analysed according to U.S. EPA 8270E 2018 method by gas chromatography/mass spectrometry (GC/MS) (U.S. EPA, 2014). The GC/MS analysis involves the introduction of SVOCs by injecting the extracts into a GC that is equipped with a slender fused-silica capillary column. The temperature of the GC column is controlled to effectively separate the targeted substances, which are then detected using a MS linked to the GC instrument. Both PTEs and PAHs data were expressed in mg/kg on the total dry weight at 105 °C.

2.5. Univariate statistics

Plots for exploratory data analysis, associated to detailed univariate statistics, were produced for all the measured variables for evaluations on the main characteristics of the distributions.

Then, for As and Sb data, that showed several rounded zeros mainly due to the proximity of the measurements to the instrumental detection limits, imputation of data was performed using the "ImpRZilr" (Imputation of Rounded Zeros Isomeric log-ratio) function, included in the "RobComposition" package (Templ et al., 2011) available for the R software. The function runs an iteratively algorithm that imputes parts with rounded zeros in each step; after all parts are imputed, the algorithm starts again until the imputations do not change anymore. After missing data estimation, the main statistical parameters describing the populations (minimum, maximum, median, quartiles, kurtosis, skewness, median absolute deviation-MAD and robust coefficient of variation-CVR) were calculated.

2.6. Multivariate analysis: Compositional/non compositional data and robust PCA analysis

Compositional data, such as geochemical data, are parts (d), carrying relative information of a single positive vector (D), generally summing to a constant value (Egozcue, 2009; Jones and Aitchison, 1987). Due to the closed structure of compositional data, standard methods of multivariate statistical analysis (e.g., Principal component and cluster analyses) based on Euclidean geometry could give misleading results (Pearson, 1896). Applying logarithm to ratios (Log-ratio transformations) (Aitchison, 1986) of compositional data resulted in a satisfactory solution to "open" data, dropping the effect of spurious correlations, and use variables for multivariate statistical analysis application relying on true correlations.

A robust principal component analysis (rPCA) was performed, through the "pcaCoDa" function (Filzmoser et al., 2009; Kynčlová et al., 2016) available in "robComposition" package in R, to explain variability and investigate the existence of relationships among multiple variables as a response to an environmental process or a human action. For the robust method, the compositional data are expressed in isometric log-ratio (ilr) coordinates (Hron and Filzmoser, 2015). Before performing the rPCA, two independent compositional datasets were identified: the first including concentration data of PTEs from the topmost layer of soil (between a depth range 0 and 15 cm from the surface) and the second relating to the samples collected at the 15–30 cm range of depths. Ilr coordinates were internally generated for each compositional group (Filzmoser et al., 2009; Hron and Filzmoser, 2015).

External non-compositional variables were appropriately centred and scaled to mean 0 and standard deviation 1 (Becker et al., 1988). Following the rPCA, the resulting loadings and scores were transformed from the ilr space to the clr space to be plotted and interpreted in a compositional biplot (Filzmoser et al., 2009; Hron and Filzmoser, 2015; Kynčlová et al., 2016).

2.7. Geostatistical analysis

The different measured soil data related to potentially toxic elements (PTEs), polycyclic aromatic hydrocarbons (PAHs), electromagnetic induction (EMI) and cone index (CI) in the study area were regarded as random functions and modelled using the methods of geostatistics (Matheron, 1963). The measured values (z) of soil data at each point $\mathbf{x}$ ($\mathbf{x}$ is the location coordinates vector) are called regionalized variables [$z(\mathbf{x})$] and are considered as the outcome of a random variable $Z(\mathbf{x})$. Pairs of these regionalized variables, $z(\mathbf{x})$, at different distances should be correlated and exhibit a certain spatial structure. The set of spatially dependent random variables $Z(\mathbf{x})$ forms the random function structure (Matheron, 1963). The spatial structure is quantified and modelled by an experimental variogram that is a function of the distance vector $\mathbf{h}$ (module and direction) called lag. The variogram quantifies how different pairs of data values become as the distance increases for defined directions. The experimental variogram consists of a set of unconnected points, and to be used to predict the variable of interest at unsampled locations, it is necessary to fit through the experimental points a continuous mathematical function (model) to calculate variogram values for any distances and not to result in negative variances for any combination of random variables (Armstrong, 1998). Range and sill are the main parameters defining each variogram model type. The range is the distance at which pairs of data values are yet spatially correlated, while the sill is the variogram value corresponding to the range (Webster and Oliver, 2007). The variogram at the origin can be different from zero and has a positive intercept. It is called the nugget effect and arises from errors of measurement and spatial variation within the shortest sampling interval (Webster and Oliver, 2007). Since could occur that different variogram models can be fitted to an experimental variogram, to choose the best model a procedure known as cross validation was used (Webster and Oliver, 2007). The goodness of compatibility of data and model was checked by calculating two statistics: the mean error (ME), which proves the lack of bias of the estimate if its value is close to 1, and the mean squared deviation ratio (MSDR), which is the mean ratio between the squared errors and the kriging variance (Webster and Oliver, 2007).

Describing and modelling the spatial structure of the variable(s) of interest is called structural analysis and it is aimed both to understand and interpreting the spatial structure in the scope to be used for given evaluation problem such as making a map. For the latter, the variogram and the set of data in one of the many variants of kriging are used for estimating values at unsampled point locations or averages over blocks (Chilès and Delfiner, 2012). The most commonly used form of kriging is ordinary kriging (OK) and, like other kriging variants, calculates the best estimate at unsampled locations, minimizing the estimation variance (or kriging variance) that provides some information on local uncertainty. However, this local uncertainty measured by the estimation variance doesn't depend on the data values but only on the geometry of data locations and on the variogram (Chilès and Delfiner, 2012). Uncertainty estimates should complement any estimated map warn potential users about the quality of soil property predictions (Padarian and McBratney, 2023). In particular, this is most necessary when it involves protecting public health or planning remediation of contaminated sites. In these cases, the suitable geostatistical tool to be used is a stochastic simulation (Matheron, 1973). The geostatistical stochastic simulation generates a large number of equiprobable images (also called realizations) that honour the sample data and reproduce their statistical characteristics and spatial features. In this study, the turning bands parametric method was used because it represents a reasonable trade-off between prediction quality and computing time (Lantuéjoul, 2002; Matheron, 1973). The number of realizations was set at 100 because a satisfactory level of

accuracy is achieved when the number of runs is sufficiently high. The turning bands method is a Gaussian simulation technique that requires a multi-Gaussian framework. Therefore, data were transformed into a normal shaped distribution variable with zero mean and unit variance, using a procedure known as Gaussian anamorphosis (Chilès and Delfiner, 2012; Wackernagel, 2003).

Since the realizations obtained from the stochastic simulation are consistent with the observed data and equally probable, then it follows that pixel-by-pixel histograms, summarising a large number of simulations, approximate the probability distribution functions corresponding to the locations. Therefore, it is possible to present a map of the 'expected' value at any given location (E-type or Expected-value estimate) and the related standard deviation as measure of uncertainty of the predictions (Journel, 1983). Moreover, the probability of not exceeding a particular threshold value can be computed from a set of realizations by counting the number of times in which the values do not exceed a stated threshold at any given location and converting the sum to a proportion. These probabilities can be presented in map form and provide the spatially varying empirical probability that can be very useful in supporting decision-makers.

The univariate case is easily extended to the multivariate one and allows to estimate or simulate multiple variables simultaneously. The multivariate variation is modelled by a linear model of coregionalization (LMC) including a variogram for each variable (auto- or direct variogram) and a cross-variogram for each pair of variables (Goovaerts, 1997). More details can be found in Goovaerts (1997), Chilès and Delfiner (2012), Webster and Oliver (2007), Wackernagel (2003), among many others.

Direct measurements of geochemical concentrations might be supplemented by secondary information, such as measurements from different proximal sensors. Generally, the estimation improves when denser auxiliary information is taken into consideration (Goovaerts, 1997). That is especially true when the attributes of interest are measured at a few sparse points or when the data are poorly correlated in space (Goovaerts, 1997). Data measured in this study might be used as auxiliary information (or covariates) in the geostatistical prediction (or simulation) to supplement sparsely sampled target properties. Among geophysical measurements, particular importance and usefulness can be gained from the apparent electrical conductivity of soil (ECa). It is measured along closely spaced transects, which allows high-resolution maps to be obtained that can be used as exhaustive variables in multivariate geostatistical approaches.

There are different kriging algorithms to incorporate exhaustively sampled secondary data. Among them, kriging with external drift (KED) (Goovaerts, 1997) was used. The basic hypothesis of KED is that the expectation of the geochemical concentrations known only at a small set of points in the study area, can be modelled by the sum of a linear function of a smoothly varying secondary (external) variable $m(\mathbf{x})$ (proximal sensing data in this case) and a spatially correlated random component $r(\mathbf{x})$ with zero mean and variogram $\gamma_r(\mathbf{h})$ (Castrignanò and Buttafuoco, 2020; Goovaerts, 1997):

$$z(\mathbf{x}) = m(\mathbf{x}) + r(\mathbf{x}) \quad (1)$$

In the scope of geostatistical analysis of geochemical concentrations in soils and for considering their compositional nature, data were submitted to a log-ratio transformation. Among those available in literature, the isometric log-ratio (ilr) transformation (Egozcue et al., 2003) has been used because of its effective and practical treatment of compositional data in the correct application of geostatistics (Tolosana-Delgado et al., 2019; Tolosana-Delgado and Mueller, 2021). After the application of the geostatistical methods, the ilr transformed data were back transformed into the raw data using the ilr inverse. The maps were obtained by interpolating or simulating all variables according to a regular grid (0.50 m × 0.50 m).

Geostatistics also makes it possible to solve the crucial problem called change of support, which arises when several variables with different support need to be analysed jointly. The complete specification of the term support includes the geometrical shape, size, and spatial orientation of the measurement volume. The support can be as small as a point or as large as the entire field. In geostatistics it is possible to solve the problem of change of support by resorting to block cokriging (Castrignanò and Buttafuoco, 2020; Gotway Crawford and Young, 2005).

Regarding the output of maps of the different soil properties, areas on the map were assigned to classes using the Concentration Area (C-A) method (Cheng et al., 1994; Sadeghi, 2023) that investigates the relationship between each pixel value (C) and the cumulative area having values greater than a specific value (A(> C)), to find anomalies with respect to the natural back-ground of the site. Classes' thresholds were determined in a log-log plot, where each pixel's value C is plotted versus the area having values greater than C, and they correspond to the inflections along the distribution curve of the points. Differently, classes for the CI spatialization were defined considering the literature (as reported in the paragraph 3.1) for root penetration limits: CI values in the ranges 1–2 MPa and 2–3 MPA identify a state of reducing and restricting root penetration, respectively, while hardened was evaluated the soil in the 3–5 MPa range. Based on the obtained data, distribution maps of the measured compositional and non-compositional variables were obtained.

All geostatistical analyses were performed using the software package Isatis.neo, release 2023.04 (Bleines et al., 2023), whereas the compositional data procedures were performed by using the software package CoDaPack 2.0 (Comas-Cufí and Thió-Henestrosa, 2011).

3. Results and discussion

3.1. Exploratory univariate data analysis

3.1.1. Electrical conductivity (ECa) and magnetic susceptibility (MSa)

Exploratory plots with univariate descriptive statistics are provided for each analysed variable to evaluate the main characteristics of the distributions. EMI plots (Fig. 2) identify clear right-skewed distributions for the electrical conductivity (ECa) measured in the volumes 0–25 cm (ECa25) and 0–50 cm (ECa50V and ECa50H, for VCP and HCP modes, respectively), which shows several lower (below 1 mS/m) and upper values for (maximum values up to 10–12.4 mS/m, respectively), while weakly right-skewed tending towards a Gaussian reveals the 0–90 cm (ECa90) distribution, with both few lower (below 3 mS/m) and upper values (above 8.5 mS/m). On the contrary, the skewness around 0 and the very similar median and mean values identify Gaussian-like distributions for the ECa measured in the 0–100 and 0–180 cm volumes (ECa100 and ECa180, respectively) (Fig. 2). About the MSa distributions (Fig. S1), evident similarity of patterns is found among data measured in the topsoil (MSa25) and the subsoil from 0 to 50 cm (MSa50V and MSa50H) and 0 to 90 cm (MSa90) that are all left-skewed and characterised by very similar mean values. On the contrary, MSa of the bottom soil from 0 to 100 and 0 to 180 cm (MSa100 and MSa180, respectively) show right-skewed distributions.

The occurrence of skewed distributions for both ECa and MSa values and different (opposite for MSa) patterns for the uppermost soil volumes compared with the lower ones evidence soil properties variability in the space and with depth that can be related to the different extent of the anthropogenic contamination in the investigated area.

3.1.2. Dose rate, K, U and Th

The mean dose-rate values (141 nGy/h) and the mean K, eU and eTh contents (3.5 %, 7 mg/kg and 22 mg/kg, respectively) (Fig. S2) are strongly consistent with data reported for the trachytic pyroclastics of Volcano Island (Dose Rate = 165.8 nGy/h; K = 3.6 %; eU = 26.2 mg/kg; eTh = 8.9 mg/kg) (Chiozzi et al., 2001). The comparison with the Volcano products has been made due to the similarity of the petrographic composition with several Somma-Vesuvius and Phlegrean Fields

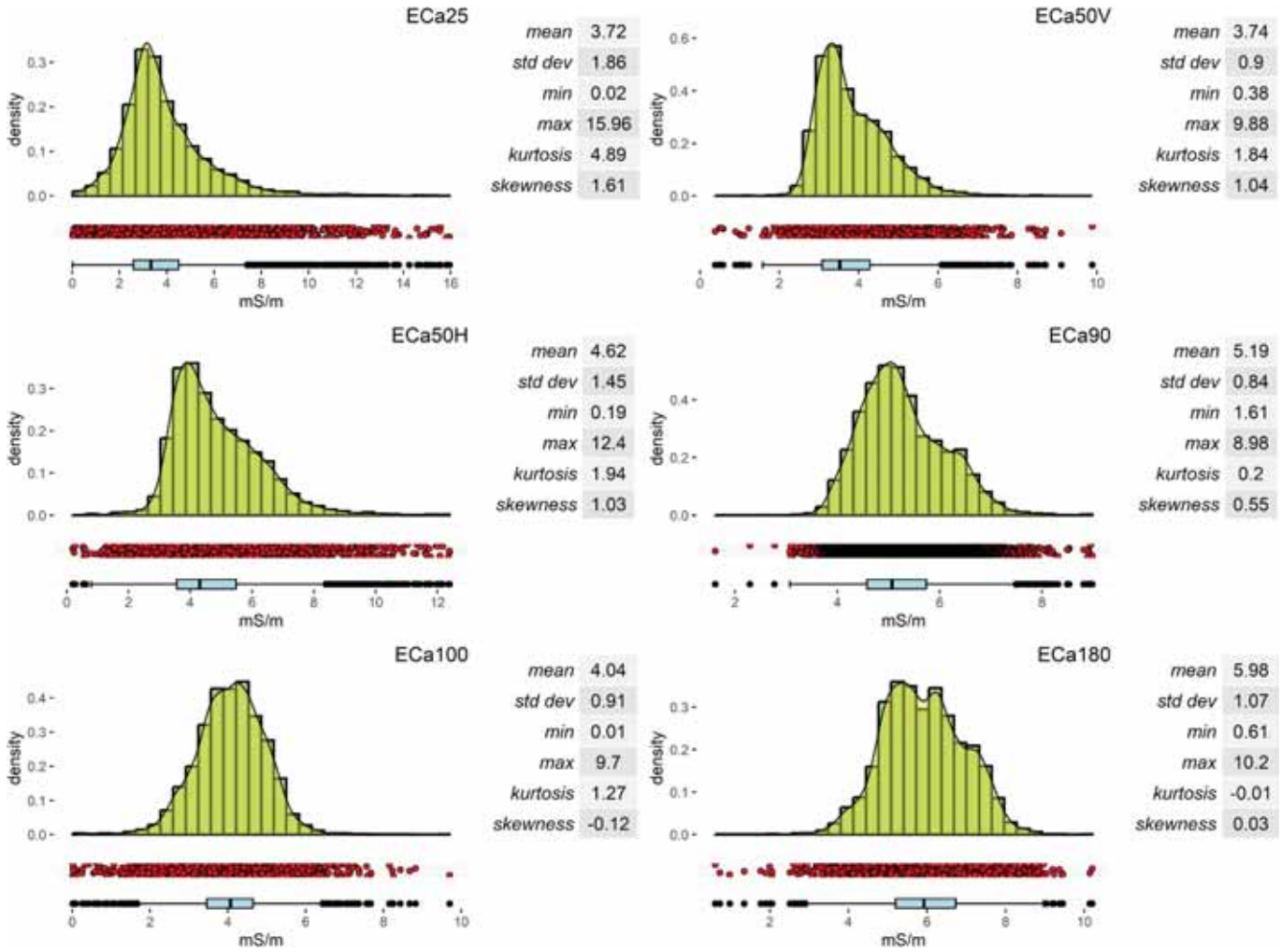

Fig. 2. Exploratory data analysis combining histograms, density and boxplots of apparent electrical conductivity (ECa) measures obtained by the EMI technique in vertical coplanar (VCP) mode for ECa25, ECa50V, ECa90 and horizontal coplanar (HCP) mode for ECa50H, ECa100, ECa180.

deposits featuring alkaline basaltic trachyandesitic and trachytic (for the Neapolitan Yellow Tuff -NYT) composition, respectively (Lima et al., 2007). On the contrary, for both dose-rate and K content (97 nGy/h and 2.9 %, respectively), the study area shows higher mean values than those measured in the nearby Marcianise industrial area (Vingiani et al., 2022). In that site, the lowest values of γ-ray emissions have been found to be significantly correlated with the most contaminated areas, where anthropic wastes emitted lower radiations compared with the more natural ones (122 nGy/h and 3.6 %). The exploratory plots (Fig. S2) show left-skewed distributions for K and Th, characterised by anomalies of lower values; high K and Th values are expected in the investigated field since K is a basic element of the potassic and ultra-potassic volcanism of Phlegrean Fields (Cannatelli, 2012; Deino et al., 2004) and Somma-Vesuvius (Ayuso et al., 1998; Lima et al., 2007), as well as the Th is a frequently occurring element in volcanic environment, and for that it has been successfully used as proxy for separating volcanic from non-volcanic parent materials (Mileti et al., 2013). On the contrary, U distribution is characterised by more centred pattern, close to a Gaussian, even then few upper anomalies (almost double of the mean value) are also found.

3.1.3. Cone index (CI) and soil thickness (ST)

For each CI series, median and maximum values are calculated on each station within 2 soil depths (0–15, 15–30) and plotted (Fig. S3), while only maximum values are reported for the CI between 30 and 60 cm (Table S1). The maximum value is used to identify the presence of thin (a few centimetres) compacted layers within the investigated depth, while the median values allow the evaluation of the average degree of compaction for a depth range of interest. In some surveyed points, the intense degree of soil compaction limited measures at 30 cm of depth, and the mean and median values for the 30–60 cm of depth were not calculated. The exploratory plot of the CI related to the 0–15 cm layer (Fig. S3) shows a right-skewed distribution with low mean (1.1 MPa) and median (0.8 MPa) values, and presence of few upper values around 4 MPa. Considering that soil compaction begins to inhibit the root growth of most plants for increasing soil strength starting from 1.42 MPa values (Blanchar et al., 1978; Duruoha et al., 2007; Rosolem et al., 1994; Taylor, 1973), this first soil layer features a normal soil state for root penetration, as expected because of probable milling practices performed in the field during the years of use as agricultural field. On the contrary, worthy of note is the increasing resistance to root penetration in the second layer (mean value of 2.7 MPa) where the CI measures have bimodal distribution, with a first group of values characterised by mean above 2 MPa and a second group centred on values between 3.5 and 4 MPa, which are typical of a hardened soil (from 3 to 5 MPa) consistently with the presence of a plow pan. Then, the average highest maximum value (4.4 MPa) is registered in the depth range between 30 and 60 cm (Table S1).

Strong bimodality is observed in the plot of the ST distribution measured by the steel rod (Fig. S3), characterised by a first group of

values with Gaussian distribution centred at 100 cm and a second group including more than a third (62) of the total measures (174) that have ST values of 200 cm or more, considering that the used steel rod is long 200 cm.

3.1.4. PTEs soil content and relationship with Italian regulation

The quality check on the accuracy of the pXRF measures, performed by certificate materials (Table S2), shows recovery of 99 and 98 % for Pb, 102 and 101 % for Cr, 88 and 101 % for Zn, 111 and 106 % for V, 83 and 101 % for As, 158 and 88 % for Sb, respectively for NIST 2710a and NIST 2711a, while for Ca, Fe and K recoveries range from 85 to 116 %.

Descriptive statistics of the PTEs measured by pXRF are reported in Table 1 for the shooting area (SA) and in Table 2 for the control samples (CS). The exploratory plots of As, Pb, Sb for both layers at 0–15 and 15–30 cm of the SA (Fig. 3) show right-skewed distributions with few upper values (not considered as outliers since of the point-based contamination), which support the anthropogenic origin of these elements. The median values for As and Sb are lower and slightly lower than the mean, respectively, consistently with the CV which is 48–30 % for the As and around 60 % for the Sb, in the two layers. On the contrary, the median values of Pb are approximately the half of the mean values in both layers, and the distributions show very high coefficient of variability (CV) (109 and 117 %, at 0–15 and 15–30 cm, respectively). Noteworthy is the right-skewed distribution of the Cr at 15–30 cm, and the maximum measured values that are greater than the double of the mean, as well as the CV around the 30 %. In addition, V and Cu distributions are characterised by generally low pronounced (from 0.25 to 0.41) right skewness, while Zn shows a bimodal distribution for the first layer data and a left-skewed distribution.

The whole element content of both SA layers was compared with the composition of in situ collected control samples (CS) at 0–15 and 15–30 cm. Sensitive differences were found mostly for Ca (15.7 and 15.4 % for CS versus 3.7 % and 5.2 % for SA), likely due to the presence of randomly distributed carbonate fragments related to the underlying travertine layers, whereas minor differences were showed by K (0.8–1.5 vs 3.1–4.9 %) and Fe (2.8- vs 1.3–1.7 %). About the PTEs, the mean content measured for the CS is always lower than that of both SA layers: As is 11 and 15 mg/kg in the CS vs 29 and 27 mg/kg in the two layers, Cr is 54 and 56 mg/kg vs 73 and 106 mg/kg, Mn is 570 and 535 mg/kg vs 790 and 1143 mg/kg, Pb is 84 and 74 mg/kg vs 878 and 844 mg/kg, Sb is below the limit of detection (LOD) vs 31 and 27 mg/kg, V is 105 and 116 mg/kg vs 127 and 136 mg/kg, Zn is 105 and 97 vs 135 and 130 mg/kg, while Cu is very similar (76 and 60 mg/kg vs 75 and 71 mg/kg). Further, the soil elemental composition of SA was also compared with the reference concentration range (RCR) determined for the topsoil of the same area in a wider regional study authored by De Vivo et al. (2021). Regarding the major elements, in both layers the mean content of Ca (3.7 % and 5.2 %, respectively) results to be quite lower than the reference area (i.e., 6.8–19 %); on the other hand, referring to the same regional study as above, Fe (2.79 % and 2.84 %, respectively) and K (3.13 % and 4.94 %, respectively) mean concentrations are roughly in line with the previously reported ranges (i.e., 2.33 %–3.59 % for Fe, and 1.19 %- 3.54 % for K), whereas Ti shows a slightly increase (3434 mg/kg and 4903 mg/k vs. a range of ca 1200 mg/kg-2000 mg/kg).

With respect to the PTEs, for both investigated layers of the SA, As (29 mg/kg and 27 mg/kg in the upper and lower layer, respectively), Cu (75 mg/kg and 71 mg/kg, respectively), and Mn (790 mg/kg and 1143 mg/kg, respectively) show local mean values which fit well with the ranges reported by De Vivo et al. (2021) (i.e., 13.4 mg/kg - 31.1 mg/kg for As, 52.1 mg/kg – 139 mg/kg for Cu, 663 mg/kg - 1223 mg/kg for Mn) (Table 3). On the contrary, Cr (73 mg/kg and 106 mg/kg, respectively), Pb (878 mg/kg and 844 mg/kg, respectively) and Sb (54 mg/kg and 79 mg/kg, respectively) are featured by mean concentrations massively above the values assessed for the area at regional scale (13.8 mg/kg – 32.1 mg/kg for Cr, 53 mg/kg −167 mg/kg for Pb, 0.43 mg/kg −1.12 mg/kg for Sb). Specifically, it is worth highlighting that Pb and Sb

Table 1
Descriptive statistics of element concentration measured by the portable X-ray fluorescence spectrometer (pXRF) on soils sampled from the shooting area (SA) at 0–15 cm ($n = 174$) and 15–30 cm ($n = 174$) of depth. LOD is the limit of detection for the pXRF measures. N is the number of measures below the LOD.

Element	As		Cr		Cu		Pb		Sb		V		Zn		Mn		Ca		K		Fe	
	mg/kg																%					
Depth (cm)	0–15	15–30	0–15	15–30	0–15	15–30	0–15	15–30	0–15	15–30	0–15	15–30	0–15	15–30	0–15	15–30	0–15	15–30	0–15	15–30	0–15	15–30
LOD	<5		<10		<10		<5		<20		<10		<5		<10			<0.005		<0.005		<0.01
N < LOD	0	0	0	0	0	0	0	0	54	79	0	0	0	0	0	0	0	0	0	0	0	0
mean	29	27	73	106	75	71	878	844	31	27	127	136	135	130	790	1143	3.7	5.2	3.13	4.94	2.78	2.84
SD	11	8	23	32	23	26	959	986	19	17	17	25	32	33	147	234	1.72	2.89	0.56	0.94	0.29	0.29
min	15	11	35	53	15	10	57	48	9	8	81	81	67	53	399	584	1.12	1.24	1.92	3.12	1.82	0.17
max	101	66	143	275	150	147	4328	6629	95	101	176	211	210	226	1196	1809	20.78	32.35	4.51	7.97	3.74	3.86
LQ	22	22	54	87	58	54	138	119	13	13	116	120	114	106	685	1001	3	4.2	2.74	4.32	2.62	2.68
median	26	25	70	101	74	70	501	464	27	21	125	135	138	133	800	1136	3.52	4.9	3.2	4.89	2.76	2.82
UQ	32	28	85	116	91	85	1196	1361	38	38	138	149	157	153	884	1272	4.1	5.65	3.53	5.33	2.96	3.00
kurtosis	12.28	5.97	0.34	4.24	0.58	0.39	1.39	7.41	1.21	2.02	0.14	0.41	−0.55	−0.12	−0.08	0.29	57.32	48.92	−0.51	1.17	1.25	2.65
skewness	2.86	1.92	0.79	1.55	0.25	0.28	1.44	2.18	1.22	1.29	0.37	0.41	−0.06	−0.02	0.12	0.31	−0.05	5.83	6.19	0.85	−0.14	−0.40
CV (%)	48	30	32	30	31	37	109	117	62	62	14	19	24	25	19	20	47	56	18	19	11	10

Mean = arithmetic average; SD = standard deviation; min = minimum value; max = maximum value; LQ = lower quartile, UQ = upper quartile, CV = coefficient of variation.

Table 2
Descriptive statistics of element concentration measured by the portable X-ray fluorescence spectrometer (pXRF) on samples ($n = 15$, analysed in duplicate) collected from potentially uncontaminated soils at two depths (0–15 and 15–30 cm), defined control samples (CS), in the proximity of the shooting area (SA). LOD is the limit of detection for the pXRF measures. N is the number of measures below the LOD.

Element	As		Cr		Cu		Pb		Sb		V		Zn		Mn		Ca		K		Fe	
	mg/kg																%					
Depth (cm)	0–15	15–30	0–15	15–30	0–15	15–30	0–15	15–30	0–15	15–30	0–15	15–30	0–15	15–30	0–15	15–30	0–15	15–30	0–15	15–30	0–15	15–30
LOD	<5		<10		<10		<5		<20		<10		<5		<10		<0.005		<0.005		<0.01	
N < LOD	0	0	0	0	0	0	0	0	30	30	0	0	0	0	0	0	0	0	0	0	0	0
mean	11	15	54	56	76	60	84	74	ND	ND	105	116	105	97	570	535	15.7	15.4	0.8	1.5	1.3	1.7
SD	3	2.9	18	10.2	14	11.0	42	15.2	ND	ND	24	22	45	18	148	98	2.7	2.6	0.2	0.3	0.15	0.3
min	7	10	25	33	59	41	48	54	ND	ND	72	72	72	61	364	307	9.0	12.7	0.6	0.7	1.1	1.1
max	18	20	83	74	100	82	198	116	ND	ND	152	147	261	145	853	668	18.8	20.8	1.4	2.1	1.5	2.2
LQ	9	12	40	52	67	52	60	63	ND	ND	86	97	83	88	453	472	15.0	13.4	0.7	1.3	1.2	1.5
median	10	15	55	57	71	58	68	72	ND	ND	109	126	93	93	567	563	16.5	14.3	0.8	1.5	1.3	1.8
UQ	12	17	65	64	86	65	86	80	ND	ND	117	135	110	106	663	610	17.3	17.1	0.9	1.7	1.45	2.0
kurtosis	1.19	−1.26	−0.86	0.04	−0.99	−0.39	3.31	1.72	ND	ND	−0.55	−1.05	11.31	1.31	−0.77	−0.30	1.59	−0.58	4.42	0.36	−0.94	−0.82
skewness	0.97	0.13	−0.09	−0.56	0.57	0.53	1.89	1.30	ND	ND	0.33	−0.53	3.20	0.70	0.12	−0.77	−1.34	0.94	1.98	−0.27	−0.12	−0.42
CV (%)	27	20	33	18	19	18	49	20	ND	ND	23	19	43	19	26	18	17	17	24	21.83	11	19.91

Mean = arithmetic average; SD = standard deviation; min = minimum value; max = maximum value; LQ = lower quartile, UQ = upper quartile, CV = coefficient of variation.

show average values up to one order of magnitude higher than the expected values, and Pb is even featured by maximum values in both layers up to two orders of magnitude greater (4328 mg/kg and 6629 mg/kg, respectively) than the reference values for the area.

Considering the past function of the investigated area as a shooting range, the comparison between the PTEs concentration with the reference values provided by the Italian environmental legislation (Law Decree 152, 2006; Ministry Decree n. 46, 2019) for the commercial/industrial land use of soils (CSC2 in Table 3), shows that only As, Pb and Sb overcome the given thresholds. In the case of As, only a low percentage of samples exceeds the CSC2 (4.6 % and 1.1 %, at 0–15 and 15–30 cm), while a higher percentage is exceeded in the case of Pb (31 % and 31.6 %) and Sb (8 % and 42.5 %). However, assuming a possible future return of the investigated area to a residential or agricultural destination, it is relevant to highlight that the actual As, Pb and Sb concentrations, in both layers overcome the thresholds reported by legislation for the public, private and residential green (CSC1) and agricultural (CSC3) soil use for a high percentage of samples (up to 80 % for As and Pb, and up to 38 % for Sb) in the case of the CSC1, as well as up to 15 % for As, up to 80 % for Pb and up to 38 % for the CSC3 (Note that CSC1 and CSC3 are the same for Pb and Sb). Furthermore, if a public, private and residential green or agricultural use is reasonably considered for the future destination of the investigated site, it is noteworthy to stress that Cr concentration exceeded the reference value which is the same for both CSC1 and CSC3 (i.e., 150 mg/kg), solely in the 15–30 cm of depth for a total of 9.2 % of the samples. V concentrations exceed the reference value which is the same for both CSC1 and CSC3 (i.e., 90 mg/kg), in almost all the samples collected at both sampling depths (i.e., 96.6 % and 97.7 % of the collected samples, respectively). Copper and Zn concentrations only exceed CSC1 (i.e. 120 mg/kg and 150 mg/kg, respectively), with a sample percentage of 4 % and 4.6 % and 29.3 % and 33.3 %, in both depth ranges respectively.

3.1.5. PAHs soil content and relationship with Italian regulation

Exploratory plots of the soil total PAHs content (Fig. S4) highlight right-skewed distributions, with mean higher than the median of 6 to 8-fold, and presence of several upper values leading to a high CV (up to 173 %) for all the measured PAHs (Table S3). Comparing the PAHs concentrations of the study area with the CSCs established for the different land uses by the Italian environmental law (Legislative Decree 152/2006, Ministerial Decree 46/2019) (Table 4) it resulted that the mean value (14.23 mg/kg) of the total content of these compounds exceeds the CSC1 (and the CSC3, which holds the same value); specifically, 11 out of the 30 collected samples (i.e., 37 % of the total) (Table 4) are not suitable for a public, private and residential green nor an agricultural land use. However, considering the past destination of the area as shooting range, none of the sample is characterised by total PAHs concentrations overcoming the CSC2 referring to a commercial/industrial use of soils. Looking at the single analyte concentrations (Table 4), generally the mean content exceeds the CSC1 and the CSC3, except for chrysene, dibenzo(*a*,*h*)pyrene and pyrene, whereas only for 4 analytes maximum concentration values were found above the CSC2. In general, all individual compounds exceed CSC1 and CSC3 in a variable number of samples ranging from 4 (13 % of the total) to 19 (63 % of the total) and from 1 (3 % of the total) to 19 (63 % of the total), respectively, with the benzo(*a*)pyrene exceeding both CSCs, in the highest number of analysed samples (i.e, 19 out of 30). The CSC2 are overcame only for benzo(*a*)anthracene (3 samples), benzo(*a*)pyrene (4 samples), benzo(*b*)fluoranthene (1 sample) and indeno(1,2,3-*cd*)pyrene (2 samples) depicting a less relevant contamination scenario in case the destination use of the area would be set as commercial/industrial.

3.2. Modelling spatial variability, mapping, and uncertainty assessment

3.2.1. ECa, MSa, CI associated with direct soil surveys (ST)

Regarding the measurements of ECa, here for the sake of simplicity,

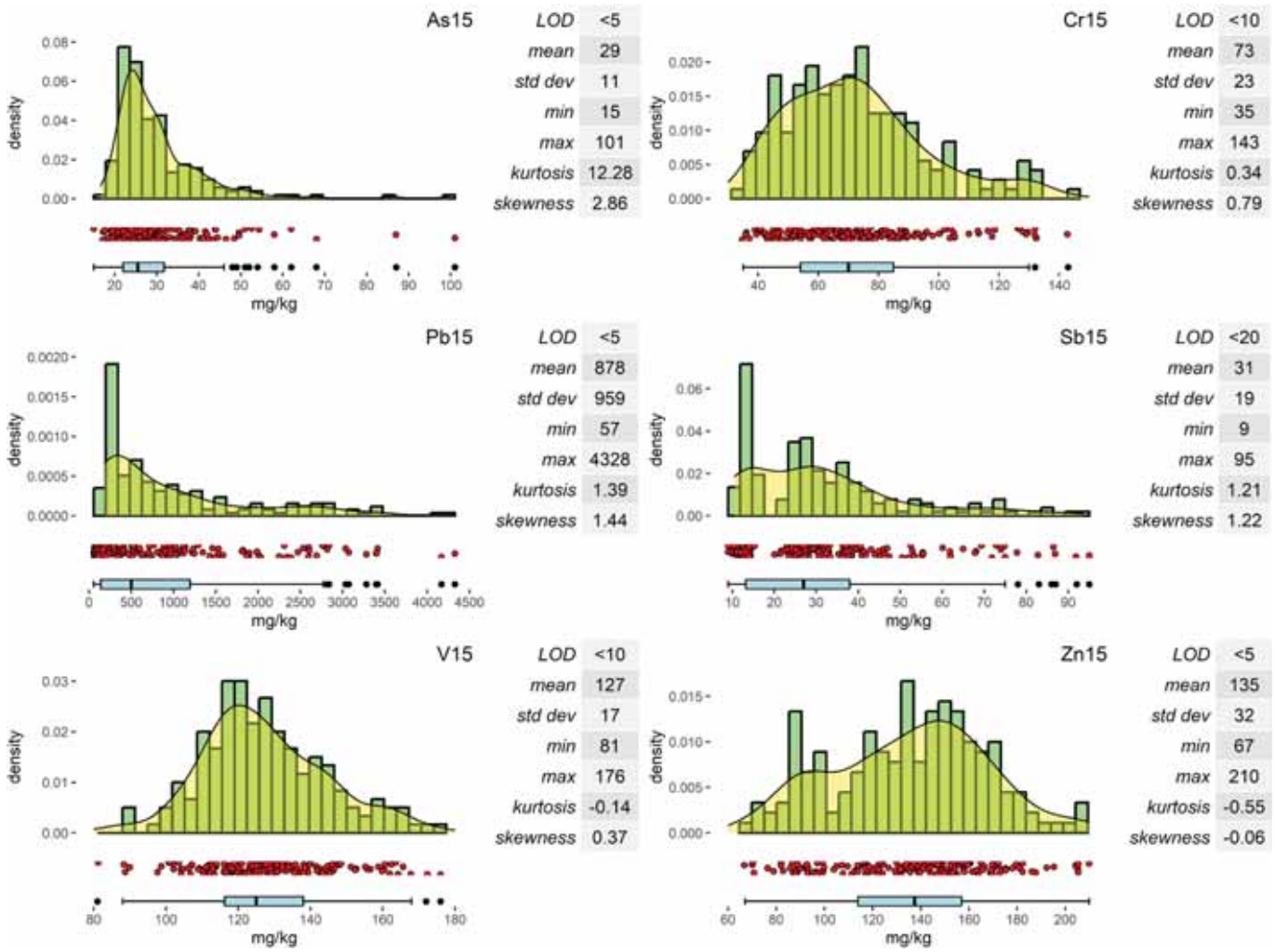

Fig. 3. Exploratory data analysis combining univariate statistics, histograms, density plots and boxplots of PTEs concentrations of the layer 0–15 cm (As15, Cr15, Pb15, Sb15, V15 and Zn15).

only the spatial distributions of ECa25 and ECa180 are reported and discussed (Fig. 4a and b). As mentioned above, ECa25 data showed an asymmetric distribution (skewness = 1.61) (Fig. 2) and since in the variogram modelling few exceptionally large values can contribute to very large squared differences, data were transformed into Gaussian shaped variable with zero mean and unit variance using the Gaussian anamorphosis procedure (Wackernagel, 2003). In the structural analysis, no anisotropic behavior was detected and an isotropic nested variogram model was fitted to the experimental variogram (Table S4). The fitted variogram model included three basic structures (nested model): a nugget effect, a spherical model at very short range (13.38 m), and a spherical model at longer range (about 88 m). The goodness of variogram fitting was evaluated satisfactory because the mean error (ME) was close to zero and the mean squared deviation ratio (MSDR) to 1 (Table S4).

The fitted variogram and the Gaussian ECa data are used with block ordinary kriging for predicting values at unsampled locations and mapping ECa25. The block ordinary kriging is used because ECa data cannot be considered point measurements. Therefore, predictions are obtained as averages over blocks (0.5 m × 0.5 m) centred at the nodes of the interpolation grid. The predicted Gaussian ECa values have been back transformed into raw data using the inverse of the Gaussian anamorphosis. The map of ECa25 is shown in Fig. 4a.

The ECa180 data didn't require any transformation into Gaussian shape because data were symmetric and skewness close to zero (Fig. 2). No anisotropic behavior was detected and an isotropic nested variogram model has been fitted to the experimental variogram (Table S4). It included two basic structures (nested model): a spherical model at short range (40.08 m), and a spherical model at longer range (85.64 m). The goodness of variogram fitting was evaluated satisfactory because the mean error (ME) was zero and the mean squared deviation ratio (MSDR) close to 1 (Table S4).

As for ECa25 data, block ordinary kriging was used to predict the ECa180 averages over blocks (0.5 m × 0.5 m) centred at the nodes of the interpolation grid (Fig. 4b).

The maps of ECa25 and ECa180 allow to identify two different patterns for the shallowest and the deepest surveyed volumes. In the ECa25 (Fig. 4a), the class of the highest values (4.3 > ECa > 11.4 mS/m) are concentrated in the eastern part of the field along a regular band NNW-SSE oriented. This regular pattern gradually modifies with depth (ECa180, Fig. 4b) where the highest values (ECa > 6.6 mS/m) enlarge from the band towards west, assuming irregular shape. Looking at the shooting positions located in the western part of the field (Fig. 1c), the regular band assuming the highest values in the ECa25 map is parallel to the positions and far from them approximately 110–150 m, indicating a clear relationship between ECa measures and shooting platform position. As reported by the literature (Binley et al., 2010; Cassiani et al., 2014), EMI geophysical survey represents a powerful tool to identify the spatial extent of contaminants distribution in soil, even though the measured signal is not directly related to the pollutant concentration,

Table 3
Reference Concentration Range (RCR) and contamination threshold concentrations (CSC) of PTEs provided by the D.Lgs. 152/2006 All. 5 and D.M. 46/2019 for areas designated to public, private and residential green (CSC1), industrial/commercial (CSC2) and agricultural (CSC3) use are reported in mg/kg. N is the number of samples exceeding CSCs, while in brackets the percentage of the total analysed samples exceeding CSCs. CS are the control samples; SA are the soils from the shooting area.

Areas	Elements	Reference Concentration Range (RCR)	Public, private and residential green use (CSC1)		Industrial/commercial use (CSC2)		Agricultural use (CSC3)	
		(De Vivo et al., 2021)	All. 5 D.Lgs. 152/2006		All. 5 D.Lgs. 152/2006		All. 2 D.M. 46/2019	
		mg/kg	mg/kg	N > CSC1	mg/kg	N > CSC2	mg/kg	N > CSC3
CS 0–15 cm	As	13.4–31.1	20	0	50	0	30	0
	Cr	13.8–32.1	150	0	800	0	150	0
	Cu	52.1–139	120	0	600	0	200	0
	Pb	53–167	100	0	1000	0	100	0
	Sb	0.43–1.12	10	0	30	0	10	0
	V	46–91	90	11 (73.3%)	250	0	90	11 (73.3%)
	Zn	63.6–137	150	1 (6.6%)	1500	0	300	0
CS 15–30 cm	As	13.4–31.1	20	0	50	0	30	0
	Cr	13.8–32.1	150	0	800	0	150	0
	Cu	52.1–139	120	0	600	0	200	0
	Pb	53–167	100	0	1000	0	100	0
	Sb	0.43–1.12	10	0	30	0	10	0
	V	46–91	90	25 (83.3%)	250	0	90	25 (83.3%)
	Zn	63.6–137	150	0	1500	0	300	0
SA 0–15 cm	As	13.4–31.1	20	154 (88.5%)	50	8 (4.6%)	30	50 (28.7%)
	Cr	13.8–32.1	150	0	800	0	150	0
	Cu	52.1–139	120	7 (4%)	600	0	200	0
	Pb	53–167	100	147 (84.5%)	1000	54 (31%)	100	147 (84.5%)
	Sb	0.43–1.12	10	167 (96%)	30	70 (40.2%)	10	167 (96%)
	V	46–91	90	170 (97.7%)	250	0	90	170 (97.7%)
	Zn	63.6–137	150	58 (33.3%)	1500	0	300	0
SA 15–30 cm	As	13.4–31.1	20	152 (87.4%)	50	2 (1.1%)	30	27 (15.5%)
	Cr	13.8–32.1	150	16 (9.2%)	800	0	150	16 (9.2%)
	Cu	52.1–139	120	8 (4.6%)	600	0	200	0
	Pb	53–167	100	144 (82.8%)	1000	55 (31.6%)	100	144 (82.8%)
	Sb	0.43–1.12	10	169 (97.1%)	30	61 (35%)	10	169 (97.1%)
	V	46–91	90	168 (96.6%)	250	0	90	168 (96.6%)
	Zn	63.6–137	150	51 (29.3%)	1500	0	300	0

Table 4
Contamination threshold concentrations (CSC) of PAHs provided by the D.Lgs. 152/2006 All. 5 for areas designated to public, private and residential green (CSC1), industrial/commercial (CSC2) and agricultural (CSC3) use are reported in mg/kg. N is the number of samples exceeding CSCs, while in brackets the percentage of the total analysed samples exceeding CSCs.

	Public, private and residential green use (CSC1) All. 5 D.Lgs. 152/2006		Industrial/commercial use (CSC2) All. 5 D.Lgs. 152/2006		Agricultural use (CSC3) All. 2 D.M. 46/2019	
PAH	mg/kg	N > CSC1	mg/kg	N > CSC2	mg/kg	N > CSC3
Total	10	11 (37%)	100	0	10	11 (37%)
b(*a*)a	0.5	14 (47%)	10	3 (10%)	1	12 (40%)
b(*a*)p	0.1	19 (63%)	10	4 (13%)	0.1	19 (63%)
b(*b*)f	0.5	14 (47%)	10	1 (3%)	1	12 (40%)
b(*ghi*)p	0.1	15 (50%)	10	0	5	1 (3%)
b(*k*)f	0.5	11 (37%)	10	0	1	11 (37%)
c	5	4 (13%)	50	0	1	12 (40%)
d(*ae*)p	0.1	13 (43%)	10	0	0.1	13 (43%)
d(*ah*)a	0.1	14 (47%)	10	0	0.1	14 (47%)
d(*ah*)p	0.1	10 (33%)	10	0	0.1	10 (33%)
d(*ai*)p	0.1	11 (37%)	10	0	0.1	11 (37%)
d(*al*)p	0.1	16 (53%)	10	0	0.1	16 (53%)
d(123 *cd*)p	0.1	16 (53%)	5	2 (7%)	1	16 (53%)
p	5	7 (23%)	50	0	5	7 (23%)

because of the generally low signal intensity produced by the modest volume fraction of PTEs, regardless the contamination level. In polluted sites, the soil contamination is frequently associated with simultaneous presence of more intense multiple signal sources, such as compacted layers producing other phenomena of hydrological nature, or related to the soil bulk density, that are detectable by the EMI sensors (McBratney et al., 2005).

Because of that, the cone index (CI) data by ultrasonic penetrometry until 60 cm, which allow detailed information on soil compaction at different depths, has been evaluated in combination with the ECa. Cone index (CI) data at both depths (CI15 and CI30 for the 0–15 and 15–30 cm layers, respectively) were skewed (Fig. S3) and then transformed into Gaussian shape distributions using the Gaussian anamorphosis. No anisotropy was evident for both variables and isotropic variogram models were fitted to the experimental semivariance data. The variogram model for the Gaussian values of CI15 included only a spherical model with a range of 105.42 m (Table S4), whereas a nested variogram model was fitted to the experimental semivariance data for CI30. It included a nugget effect and a K Bessel model with a range of 127.86 m and a gradient parameter of 3.80 (Table S4). The latter is a specific parameter for K Bessel model, which affects the form of the model. The cross-validation results were satisfactory for both models although the MSDR for CI15 was not close to 1, but within the typical tolerance that in this case was between 0.5 and 1.5. The fitted variograms and the Gaussian CI data for both depths are used with ordinary kriging for predicting values at the nodes of the interpolation grid. The predicted CI values were then back transformed into raw data using the inverse of the Gaussian anamorphosis. The maps of CI15 and CI30 are shown in Fig. S5. From a visual inspection, the maps show a spatially continuous highly compacted layer at 15–30 cm ($3.5 > CI > 4.1$ MPa) and a hardened root impeding layer ($2.6 > CI > 3.2$ MPa) at 0–15 cm depth ranges, respectively; both layers are characterised by NNW-SSE orientation and are placed in the eastern part of the surveyed field. Position and orientation of both compacted layers are highly consistent with the band of the highest values found in the ECa25 map (Fig. 4a).

The spatial variability of the soil thickness (ST) measured by the steel

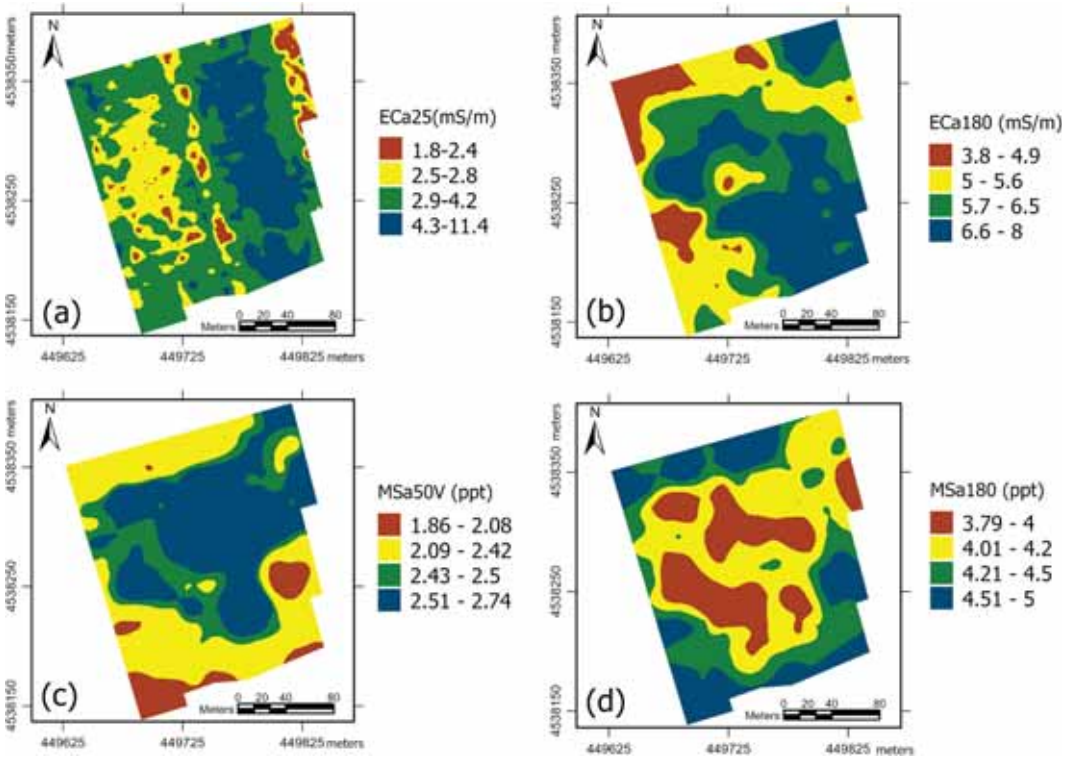

Fig. 4. EMI maps of the apparent electrical conductivity (ECa) and magnetic susceptibility (MSa). In a) ECa of the 0–25 cm topsoil (ECa25) and in b) ECa of the 0–180 cm bottom soil (ECa180); in c) MSa of the 0–50 cm upper soil (MSa50V) measured in vertical coplanar mode, and in d) MSa of the 0–180 cm bottom soil (MSa180).

rod has been also modelled and mapped. The ST data were transformed into a Gaussian distribution and no anisotropy was detected in the structural analysis. Therefore, an isotropic nested variogram model was fitted to the experimental variogram including two basic structures: a nugget effect and a spherical model with a range of 68.13 m (Table S4). However, it should be noted that the nugget effect accounts for about half of the total variability (total sill) and therefore about half of the variability of ST is unstructured. However, the goodness of variogram fitting was evaluated satisfactory because the mean error (ME) was close to zero and the mean squared deviation ratio (MSDR) close to 1 (Table S4). Finally, the fitted variogram and the Gaussian ST data were used with ordinary kriging for predicting values at the nodes of the interpolation grid and the predicted values were then back transformed into raw data using the inverse of the Gaussian anamorphosis (Fig. S6).

The spatial variability of the ST has been evaluated in association with the characteristics of the materials/soil sampled by core drillings (Tables S6a and S6b), whose location is reported on the map (Fig. S6). In the northern zone of the field, the ST is generally low (approximately 70–90 cm) in correspondence of hard travertine layers starting from an average depth of 80 cm from the surface (in A1, B1, B2, B6, C7 drilling cores). However, the travertine layers do not always represent a limiting factor for the rod deepening. In fact, in some drillings (such as B3 and C6 cores), although the travertine layers were described in the core, their thin thickness allows to be easily broken by the steel rod, and a final missing check. This hypothesis is supported by the Pz3 and Pz1 deep stratigraphy (Table S5b) showing, respectively, a deep travertine layer between 90 and 250 cm (160 cm deep) in the area close to A1 and a thin travertine layer between 80 and 140 cm (60 cm deep) close to C6.

On the contrary, in the southern zone of the field the drilling cores do not evidence occurrence of travertine layers within 100 cm of depth, but data measured by the steel rod reveals difficulty of penetration starting from 100 cm. Consistently, data of the deep Pz2 stratigraphy show presence of soil until 100 cm and presence of alluvial volcanic sand containing heterometric carbonate gravels from 100 to 250 cm. In addition, soil profiles dug in this area until 150 cm of depth (data not shown) show presence of heterometric chaotic tuff blocks in the first 30 cm, supporting the presence of obstacles to soil penetration in the southern zone as checked by the steel rod.

Noteworthy is the high consistency of patterns between the ECa180 with the ST maps (Figs. 4b and S6, respectively). This is very likely due to the higher soil moisture content and the water storage capacity of the deeper volcanic soils compared with the thin volcanic soils overlapping the travertine rocks. Otherwise, the influence of the soil moisture on the ECa is reported (Corwin and Lesch, 2005a; Sadatcharam et al., 2020).

Similar to what was done for the ECa, among the magnetic susceptibility measurements (MSa) the modelling and mapping results are only presented for the MSa50V (MSa with an effective investigation depth of 50 cm, measured in VCP) and for the MSa180 (MSa with an effective investigation depth of 180 cm). Although they were not characterised by a marked skewness (Table S4), the visual examination of the histograms (Fig. S1) suggested their regularisation through a transformation into a normal distribution. No anisotropy was evident for both MSa50V and MSa180 Gaussian data and two isotropic variogram models were fitted to the experimental semivariance data. For the Gaussian values of MSa50V, the nested variogram model included a spherical model with a range of 40.99 m and a second spherical model at longer range (110.30 m) (Table S4). For the Gaussian values of MSa180, the nested variogram model included the same structures: a spherical model with a range of 37.21 m and a spherical model at longer range (122.75 m) (Table S4). The results of cross-validation were satisfactory for both models with the mean errors (MS) close to zero and the MSDRs within the typical tolerance values.

Finally, the fitted variograms and the Gaussian MSa50 and MSa180 have been used with block ordinary kriging for predicting the averages values over blocks (0.5 m × 0.5 m) centred at the nodes of the interpolation grid. The predicted MSa values were then back transformed into raw data using the inverse of the Gaussian anamorphosis. The maps of MSa50 and MSa180 evidence very different patterns of MSa values

(Fig. 4c and d). For the upper soil (MSa50V), the observed trends are consistent with the ST and the travertine layers depth (Fig. S6). In fact, low MSa values (between 2.09 and 2.42 ppt) are found in correspondence of shallow travertine layers occurring within 80 cm of soil depth (Pz3 stratigraphy, Table S5b) in the north-western zone, while the lowest MSa values are found for the"alluvial materials of volcanic origin including calcareous fragments" occurring in the soil starting from 100 cm below the ground in the southern zone, as described for the Pz2; moreover, the highest MSa values occur in the central zone where the deepest volcanic soils are found (C1, C2, C3, C4,C9, B3, B7, B8). As reported by the literature, igneous rocks are naturally enriched of paramagnetic and magnetic minerals and measures of MS are one order of magnitude higher than sedimentary rocks, like limestone and sandstone (Carmichael, 2017; Reynolds, 1997). Accordingly, soils developed from igneous rocks have relatively higher MSa values than soils developed from metamorphic and sedimentary rocks, and the most well-known ferrimagnetic minerals in soil are magnetite, maghemite, pyrrhotite, and greigite (Mullins, 1977). Soil magnetic properties have also been used as low-cost proxy for the identification of volcanic and non-volcanic soils in the Calabria region (southern Italy), for the high correlation between MS and andic properties (Vingiani et al., 2014). The reverse pattern observed in the MSa180 map (Fig. 4d) is likely due to the increasing influence of deeper travertine layers, that caused decrease of MSa signal.

3.2.2. K, eU and eTh

Each of the three geochemical concentrations (K, eU, and eTh) and the dose-rate measured by γ-ray spectrometry have been spatially modelled individually. The distribution of the three geochemical concentrations was particularly asymmetrical for K and eTh and to a lesser extent for eU (Fig. S2). However, the data of the three geochemical concentrations were transformed into a Gaussian distribution. From the structural analysis, there was no anisotropic behavior evident for any of the three geochemical concentrations and therefore three nested isotropic models were fitted to the experimental variograms. The nested variogram model for K included three basic structures: a nugget effect and two spherical model a shorter (17.59 m) and longer range (91.89 m) (Table S6). The nested model of Gaussian data of eU included two basic structures: two spherical models at shorter (51.84 m) and longer range (515.25 m) (Table S6).

Finally, the nested variogram model for the Gaussian values of eTh included two basic structures: a nugget effect and a spherical model with a range of 167.76 m) (Table S6). The cross validation provided satisfactory results about the goodness of variogram fitting (Table S6). All MEs values were close to zero for the three nested variogram and the mean squared deviation ratio (MSDR) equal to 1 for K, very close to 1 for eTh and within the tolerance values for eU (Table S6).

Then, the fitted variogram and the Gaussian data for K, eTh and eU were used with ordinary kriging for predicting values at the nodes of the interpolation grid and the predicted values were then back transformed into raw data using the inverse of the Gaussian anamorphosis (Table S4).

Looking at the maps (Fig. S7), generally the highest content of K (approximately 3.8–4.5 %) and eTh (23.1–26.9 mg/kg) are found in the middle-northern zone of the field and in the south-western zone. The first area is in correspondence of the "arginello", where the in-situ survey evidenced outcropping yellow tuff blocks. About the second zone, scattered tuff blocks were identified at 30 cm of depth during the soil profile campaign (data not shown). Hot spots of γ-ray emissions are consistent with tuff blocks occurrence in the subsurface soil, because of their high natural radioactivity confirmed by direct measures carried out on several outcropping tuff blocks in the area, providing mean values of K equal to 9.22 %, eTh and eU equal to 36.4 and 8.65 mg/kg, respectively, and dose rate of 260.53 nGy/h. As expected, these values are higher than those measured in-situ where tuff blocks likely occur in the soil, due to the attenuating effect of the embedding soil. However, the maps obtained by the γ-ray survey do not show similarity with those obtained for ECa and MSa, ultrasonic penetrometer (CI) and the steel rod (ST). Natural emission of γ -rays from the soil is mainly related to the mineralogy of the soil parent material (Schuler et al., 2011; Martelet et al., 2013; Callegari et al., 2013). According to previous studies (Cook et al., 1996; Grasty, 1975), the γ -ray spectrometry is highly performant for studies concerning topsoil properties, since 90 % of the measured γ-radiation is emitted from about 0 to 30 or 50 cm of the soil (Beamish, 2013). Furthermore, γ-ray spectra are strongly influenced by the amount and nature of surficial stoniness (Priori et al., 2014). Therefore, since the travertine layers start to occur below 75 cm of depth, they do not produce signal anomalies as done by the surficial tuff blocks.

3.2.3. PTEs

A preliminary analysis of the PTEs made it possible to define the elements to be spatially modelled together and the possibility of using secondary information more densely measured than PTEs to improve the PTEs estimations. The first condition for jointly modelling some of the PTEs and any more densely sampled secondary variables is the occurrence of a linear relationship. In Fig. S8, the coefficients of linear correlation between the proximal and the laboratory measured variables are reported. Considering the topsoil (0–15 cm), satisfactory correlation was found between As, Pb and Sb. The relationship between Pb and Sb was higher (0.93) and predictable as it was associated with the activity of the shooting area. Indeed, Pb and Sb are PTEs contained in the bullets of the weapons used. Regarding the other more densely available measurements, among the EMI variables, the ECa25, ECa50V and the ECa50H were the most correlated with As, Pb and Sb. Similar results about the linear relationship were obtained for the lower soil layer (15–30 cm): higher correlation between Pb and Sb (0.91) and correlation of As, Pb and Sb with ECa25, ECa50V and the ECa50H (Table S6). Considering that the soil depth investigated for the PTEs concentration measure is 0–30 cm, the ECa25 was the most suitable to be used as external covariate for similarity of investigated depth.

The analysed PTEs are only parts of a whole and, as it was explained in the Materials and methods, a compositional data analysis approach was used. Moreover, since only three PTEs (As, Pb, and Sb) exceeded the CSC for industrial/commercial land use, a complementary component (filler, which will be denoted as F) was calculated to ensure the composition sums to a constant at any given location. Therefore, the three PTEs and the Filler were transformed in three isometric log-ratio coordinates (ilr.1, ilr.2, and ilr.3) and used for the following analysis. The occurrence of a linear relationship between the log-ratio coordinates and ECa25 was confirmed with satisfactory coefficients of correlation (0.68–0.70). Moreover, all ilr coordinates and ECa25 were transformed to normality and standardized to zero mean and unit variance using the Gaussian anamorphosis and such transformed data were used for all subsequent analyses.

The structural analysis required modelling a linear coregionalization of the Gaussian ilr coordinates calculating 6 (for $N = 3$; $3\times(3 + 1)/2$) direct (or auto) and cross variograms (a direct variogram for each ilr and a cross variogram for each pair of ilr). The variograms showed different variation along the direction of the transects and in the direction orthogonal to them. Indeed, along the transects (about 340° from the north clockwise and hereafter referred to as N160) the variation was continuous with a slow increase in the values of the semivariances (Fig. 5a), while along the direction orthogonal to them (70° from the north clockwise and hereafter referred to as N70), the increase was more rapid and the variograms reached higher sills (Fig. 5a). This direction matches the shot trajectory from the shooting positions (delimited by the solid red line in Fig. 1c) to the targets at the centre-western area (zone 2 in Fig. 1c). Such a spatial structure further confirms the anthropogenic origin of these elements and the resulting soil contamination.

The fitted LMC included a nugget effect, a cubic model (Webster and Oliver, 2007) with a range of 170.67 m in the direction N70 and a spherical model with a range of 145.51 m in the direction N340

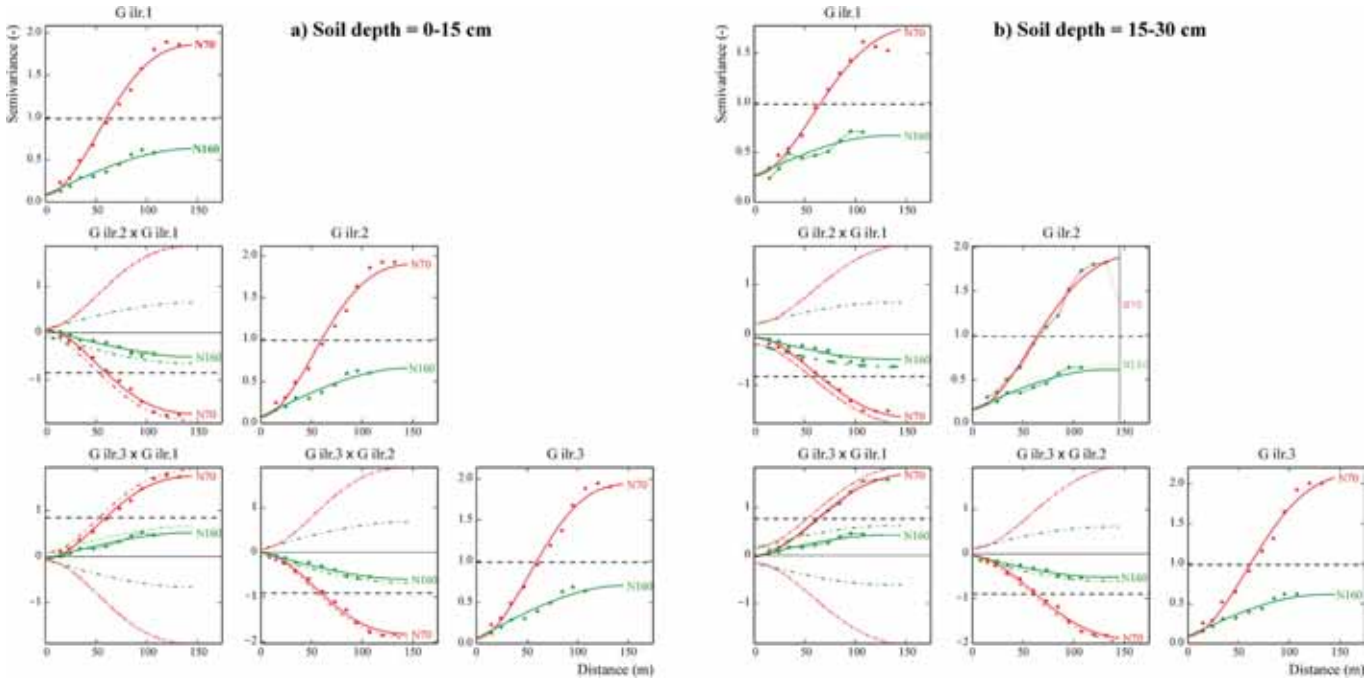

Fig. 5. Direct and cross-variogram models (thick solid red and green lines) of the linear model of coregionalization (LMC) for Gaussian values of isometric log-ratio coordinates (ilr.1, ilr.2, and ilr.3) for (a) 0–15 cm and (b) 15–30 cm soil depths. The plotted points are the experimental values whereas the solid lines are the model of coregionalization. The dashed dotted lines are the hull of perfect correlation while the horizontal dashed lines are the experimental variances.

(Table S6). From the cross-variograms (Fig. 5a), proximity of the variogram model to the dotted curve (hull of perfect correlation) representing the maximum correlation between the two variables (intrinsic correlation) (Wackernagel, 2003), the significant spatial correlation between ilr coordinates can also be deduced.

Finally, the results of cross-validation showed good reproducibility of ilr coordinates data with mean errors (ME) very close to 0 and the mean squared deviation ratios (MSDR) to 1.

Table S6 reports the decomposition of the coregionalization matrix by principal component analysis in the regionalized factors (F) for the Gaussian values of the three isometric log-ratio (ilr) coordinates for the three structures. For each regionalized factor (F), the loadings for each ilr coordinate are reported as well as the eigenvalues (EV) and the percentage of explained variance (Var. %). The elements of the regionalized factors represent the contribution of the ilr coordinates to each regionalized factor. An element with a value near 1 means that the ilr coordinate makes a large contribution to that regionalized factor. Conversely, an element near zero has a small contribution to that regionalized factor.

The nugget effect was omitted by the analysis because is mostly affected by experimental errors and spatial variation within the shortest sampling interval.

The first factor corresponding at the cubic model produced the highest eigenvalue (Table S6) and accounted for almost 100 % of the spatial variability at this direction and scale of variability (170.67 m). The first regionalized factor may be considered as a new variable which aggregates and summarizes the joint variability in the three ilr coordinates. Moreover, the elements of this first regionalized factor made a similar contribution to it because their values are similar and range between 0.57 and 0.58 (Table S6). That means that all ilr coordinates contributed similarly to the first regionalised variable without any of them having a dominant weight.

The first factor corresponding at the spherical model produced an eigenvalue of 1.7 and accounted for almost 99 % of the spatial variability at this direction and scale of variability (145.51 m) (Table S6). For this regionalised factor as well, the elements of this first regionalized factor make a similar contribution to it because their values are similar and any of them have a dominant weight (Table S6).

The Gaussian data of ilr coordinates and the LMC were used for mapping the three ilr coordinates using Kriging with ECa25 as external drift (KED). To account for the different support size of ilr coordinates data (punctual support) and the one of ECa25 data (support cannot be considered punctual), the LMC was regularized, and the predictions were averages over blocks centred at the node of the interpolation grid (0.5 m × 0.5 m). Then, the KED predictions of ilr coordinates were transformed into their raw PTEs and Filler values. The maps of As, Pb and Sb (0–15 cm depth) are reported in Fig. S10. The maps clearly reproduce what had resulted from the structural analysis, which showed a variation that reproduced the pattern of skeet shooting with a greater variation of geochemical concentrations along the shooting trajectories and much less in the direction orthogonal to them. The maps of As, Pb and Sb were complemented by uncertainty estimates obtained from their realizations generated by Turning band simulation (TBS). To do that, the Gaussian data of ilr coordinates and the LMC were used to generate 100 realizations of ilr coordinates by using Turning bands simulation using ECa25 data as external drift. Then, the 100 realizations of ilr coordinates were transformed into their raw As, Pb and Sb values and the different statistical values for each of them were calculated: the estimated expected values (E-type estimate) and the standard deviations. As already explained, the 100 simulations must be viewed as statistically indistinguishable alternative realizations of the underlying, but unknown, real world. The differences among the 100 simulated realizations of each As, Pb and Sb (0–15 cm depth) can provide a measurement of the spatial uncertainty. In Fig. 6, the maps of the means (expected values) (a, b, c) and standard deviations (d, e, f) values of As (a, d), Pb (b, e) and Sb (c, f) concentrations at 0–15 cm-depth obtained by turning bands simulations (TBS) are reported.

Regarding the PTEs at 15–30 cm soil depth, the spatial structure of the three coordinates ilr is substantially reproduced and the LMC is also modelled with the same structures (Fig. 5b and Table S6). Only ranges for the cubic and spherical models were a little different. Particularly, the range of the cubic model was greater than for Gaussian ilr

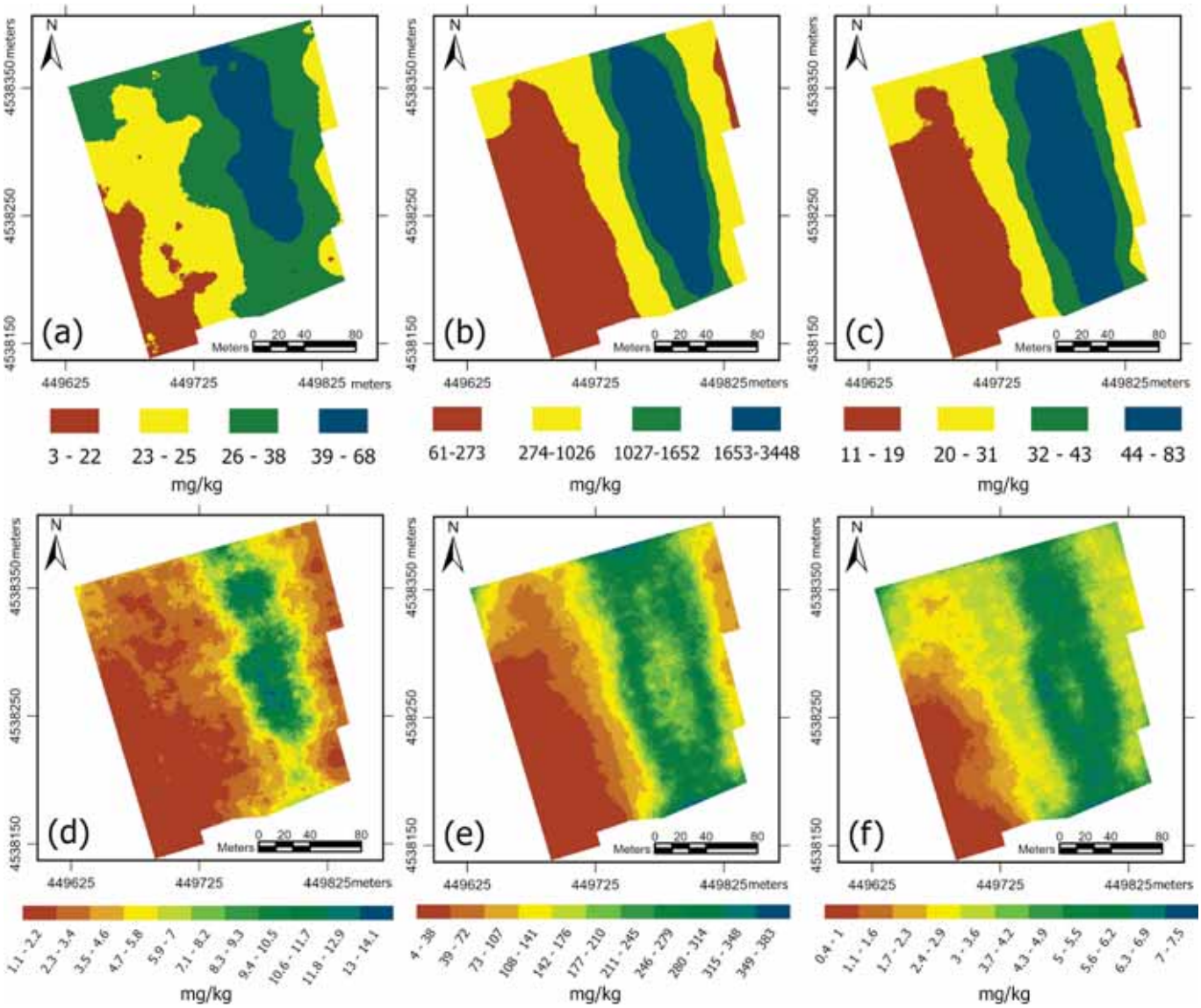

Fig. 6. Maps obtained by the mean (expected values) concentration values of (a) As, (b) Pb and (c) Sb, for the layer 0–15 cm, after turning bands simulations (TBS). Maps of the standard deviations values are reported in (d) for the As (e) for the Pb and (f) for the Sb.

coordinates at 0–15 cm, whereas the range for the spherical model was shorter than for Gaussian ilr coordinates at 0–15 cm.

The first factor corresponding at the cubic model produced again the highest eigenvalue (Table S8) and accounted for almost 100 % of the spatial variability. Moreover, among the elements of this first regionalized factor, G ilr.3 made the highest contribution to it (0.62), followed by G ilr.2 (0.58) and G ilr.1 (0.53) (Table S8).

The first factor corresponding at the spherical model produced an eigenvalue of 1.4 and accounted for almost 99 % of the spatial variability (Table S6). Also, for this regionalised factor, G ilr.3 made the highest contribution to it (0.61), followed by G ilr.2 (0.58) and G ilr.1 (0.54) (Table S6).

Finally, the Gaussian data of ilr coordinates and the LMC were used for mapping the three ilr coordinates and then obtaining the maps for As, Pb, and Sb (not shown) using the same approach than before for the G ilr coordinates at 0–15 soil depth. The maps of As, Pb and Sb were also complemented by uncertainty estimates (Fig. S9) obtained from their realizations generated by Turning band simulation (TBS).

The geochemical concentrations were lower in the 15–30 cm layer with a similar spatial distribution than in the 0–15 cm layer. In the scope to show the differences between the geochemical concentrations in the two soil depths, in Fig. S10 the maps of differences between the As, Pb, and Sb estimated at 0–15 cm and 15–30 soil depths are reported. In the study area, the geochemical concentrations in the 15–30 cm soil layer were lesser than in the 0–15 cm in the following percentages: arsenic for 52.12 % of the field, lead for 34.47 %, and antimony for 26.69 %.

Regarding the spatial uncertainty, for both soil layers investigated, the values are always low with a few areas of higher values (Figs. 6 and S9). This is evidently due to the regular distribution of the sampling locations and sampling density in relation to the size of the study area, which allowed for a good modelling of the spatial variability. A further step in this study could be to define the minimum number of sampling points that would allow modelling the variability of geochemical concentrations while maintaining an adequate level of accuracy of their predictions.

3.2.4. PAHs

Unlike all other measurements, concentrations of total polycyclic aromatic hydrocarbons (PAHs) were only determined in the laboratory on 30 soil samples according to a sampling design with a less dense grid than that used for the other measurements, which nevertheless covers the study area. Despite the sparse number of soil samples, it was possible

to model and quantify the spatial distribution of PAHs concentrations.

The distribution of PAHs concentrations was particularly asymmetrical (skewness = 2.07) (Fig. S4) and PAHs data were transformed into a Gaussian distribution using a Gaussian anamorphosis.

No anisotropic behavior evident from the structural analysis and a nested isotropic model was fitted to the experimental variogram including three basic structures: a nugget effect and two spherical model at shorter (78.36 m) and longer range (172.23 m) (Table S4).

The cross validation provided sufficient satisfactory results about the goodness of variogram fitting (Table S4) with the mean error (ME) close to zero, whereas the mean squared deviation ratio (MSDR) not very close to 1, but however, within the tolerance values (Table S4).

Focusing on the spatial patterns of the total PAHs, their variability (Fig. S11) highlights that most of the higher concentrations are located close to the shooting platform with values well above 10 mg/kg which correspond to the reference values for both CSC1 and CSC3.

Concentrations of total PAHs regularly decrease towards the east of the shooting range moving far from the platforms (Fig. S11). Noteworthy, the areas with the highest total PAHs values are likely to correspond to those which in the shooting range are crossed by the trajectories of the clay pigeons used as targets. Traditional clay pigeons were made of fired clay but, since too resistant to the shot impact, they were rapidly replaced by mixtures of carbonate powders and tar, as more fragile than the former. The main manufacturers of these products generally certify the use of non-toxic paints (EN 71–31,994) (also used in toys manufacture), plastic mixtures containing calcium carbonate and a binder, that is generally obtained from distillation of coal tar at high temperature. The binder is a black solid substance with a softening point from 30° to 180 °C, primarily composed of a complex combination of three- or more-membered condensed ring aromatic hydrocarbons generally containing no >30 mg/kg polycyclic aromatic hydrocarbons and <5 mg/kg benzo(*a*)pyrene (ARPAV, 2014). Therefore, the PAHs distribution pattern is quite consistent with the area of the shooting range where hit, break, and disintegration of clay pigeons occur, dispersing their residues on the ground and very likely determining the accumulation in soil of these compounds.

3.3. Robust principal component analysis (rPCA)

The rPCA has been performed with the aim to identify relationships among the surveyed variables as a response of both environmental processes and/or human action. The significance of correlations was tested by Pearson (Fig. S8). In the rPCA were included only the PTEs exceeding the regulation thresholds for the commercial/industrial land use (As, Pb, Sb) and the PAHs, while the significantly correlated variables obtained by the proximal sensing surveys, including the electrical conductivity of the top soil (ECa25), electrical conductivity and magnetic susceptibility of the bottom soil (ECa180 and MSa180), median cone index of the layers 0–15 and 15–30 cm (CI15 and CI30, respectively), total radioactivity (calculated as sum of all the cps measured by the scintillator) and the ST, were added to the multivariate model as external non-compositional variables (Kynčlová et al., 2016). The spatial distribution of the data of the first three components (i.e., PC1, PC2, and PC3) was quantified and modelled for their mapping and interpretation. Univariate variographic analysis of each PC revealed differences among the PCs in both the pattern of variability and the maximum distance (range) within which pairs of values from each PC were still spatially correlated. In fact, a nested model including a nugget effect and a Gaussian model with a range of 169.62 m was fitted to the experimental semivariance values of PC1. For the PC2 a nested model was fitted to its experimental semivariance values. The nested model included two spherical models with a shorter range of 47.57 m and 135.83 m. Finally, a spherical model with a range of 101.42 m was fitted to the experimental values of semivariance for PC3 data. The fitted models differ also for spatial continuity, which is greater for Gaussian model than for spherical model. Moreover, the PC2 data showed a nested structure with two scales of spatial variability.

The goodness of fitting was checked by cross validation and the two error statistics showed satisfactory results. The ME values ranged between 0.082 and 0.0308, whereas MSDR values were between 1.03 and 1.20 within the tolerance values (Table S4). PCs data and the above fitted variogram models were used with ordinary kriging to produce the maps of the first three PCs. The PC1, PC2 and PC3 account for 42 %, 12 % and 9 % of the total variability, and loadings of variables for each of them are reported in Table 5. The biplot of the first two components of the rPCA, with the individual sample observations categorized according to their distance from the shooting platform, is reported in Fig. 7. Assuming a loading cut-off value of |0.3| for the selection of the most influential variables for each component (Table 4), the PC1, PC2 and PC3 are featured as follow.

The first component (PC1) is characterised by the association made by PAHs (loading = 0.64), contrasting the Pb15 (loading = −0.42), CI (loadings from −0.26 and − 0.32, for CI15 and CI30, respectively) and ECa25 (loading = −0.28). In detail, the PAHs have the highest loadings for the PC1 and opposite sign with respect to all the other considered covariates. The negative loadings of the CI variables in the component, consistently with the Pb, are likely due to the coexistence of surficial soil contamination with high degree of compaction for the transit of heavy vehicles that collected bullet fragments from the field after shooting sessions, or to agricultural use of the area after the shooting activities. Then, worthy of note is that the ECa25 has loading values only slightly below |0.3| highlighting a clear coincidence with the vectors of Pb and CI. The ECa has been already identified as marker of PTEs contamination in industrial soil, as well as the soil compaction (Vingiani et al., 2022). The samples characterised by the highest scores for the PC1 are generally those collected far from the shooting platforms, in the eastmost sector of the study area, as can be seen from the biplot (Fig. 7) displaying the PC1 and PC2 components with the individual sample observations distributed according to their distance from the shooting platforms, and the interpolated map of the PC1 scores (Fig. 8). Although much lower than the loading cut-off value of |0.3|, it is remarkable that As15, Sb15 and Pb30 vectors show the same directions of all the above-mentioned variables. Therefore, this component can be interpreted as representative of the contamination by Pb and of the possible relationship between the Pb contamination in soil and several co-variates, including EMI variables (e.g., ECa25) and soil compaction (all CI values).

The second component (PC2) is characterised by the association of MSa180 (loading = 0.59), contrasting with ECa180 (loading = − 0.54) and ST (loading = − 0.52)(Table 5). The anticorrelation between MSa180 and ST can be explained considering that, being the ST presumably the depth of the underground travertine layers and the MS mainly related to the presence of ferrimagnetic volcanic minerals, when a deeper volume (approximately 180 cm) is investigated the presence of

Table 5
Loadings of the first three components (PC1, PC2 and PC3) resulting from the rPCA multivariate analysis.

Variables	PC1	PC2	PC3
	Loadings		
PAHs	0.643	0.221	0.317
Pb15	−0.416	−0.060	0.009
Sb15	−0.177	−0.065	−0.116
As15	−0.050	−0.097	−0.211
Pb30	−0.223	0.023	0.127
Sb30	0.043	−0.008	−0.036
As30	0.180	−0.015	−0.091
Soil Thickness	−0.118	0.523	−0.041
MSa180	0.039	−0.593	0.187
ECa25	−0.278	−0.091	0.088
ECa180	−0.156	0.538	0.109
CI15	−0.261	0.057	0.451
CI30	−0.321	0.029	0.299
Total Radioactivity	0.085	−0.081	0.684

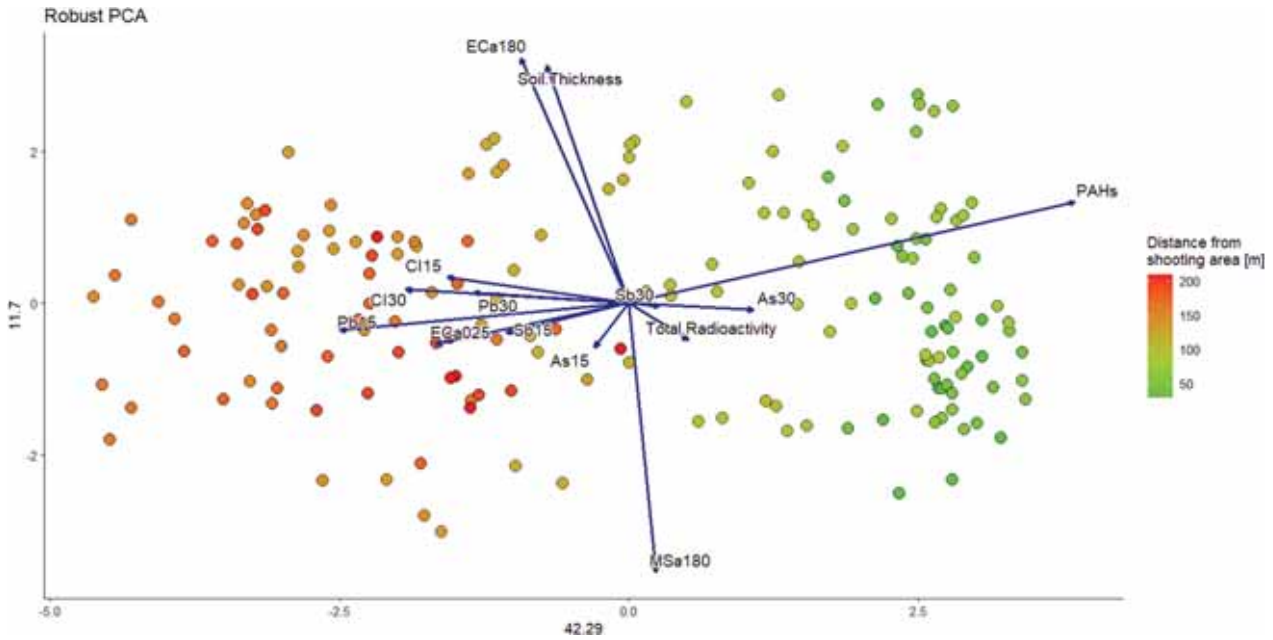

Fig. 7. Clr-biplot of the variables (n = 14) used for the robust principal component analysis (rPCA). The plot displays the PC1 and PC2 components with the individual sample observations distributed according to their distance from the shooting platform.

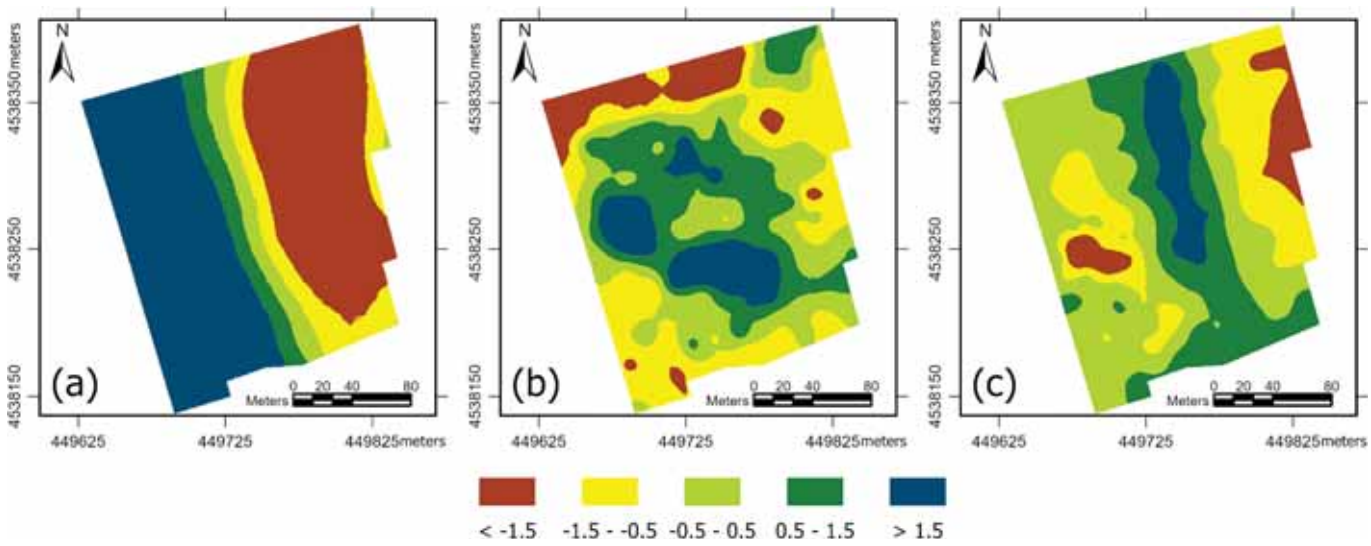

Fig. 8. Maps of the scores calculated for the first principal components (a) PC1, (b) PC2 and (c) PC3. Estimation was obtained by ordinary kriging.

the travertine bearing calcite, having diamagnetic properties, decreases the whole measured MSa. This is consistent with that observed in the map of the upper soil (MSa50V, in Fig. 4c), where the volcanic minerals of the deep soils produce high MSa values where high ST are measured. Furthermore, this interpretation is supported by the fact that both ECa180 and ST are positively signed in this association (contrary to the MSa180) consistently with the condition that deeper the travertine layer increased is the soil moisture content. This is particularly true in the investigated area where volcanic soils/Andosols are present, since of their peculiar high water-retention capacity (Nanzyo, 2002), that influence the soil water storage and then the soil moisture content, which is a parameter directly affecting the soil EC. Considering all this, we can assume the PC2 as a good marker of the soil stratigraphy as well as of the underground presence of travertine layers (or at least travertine blocks), as confirmed by the partial spatial correspondence of the highest value of PC2 scores (Fig. 8 bc) with those drilling points where travertine was found within 1 m of depth from the surface (Fig. S6).

The third component (PC3) features the presence of the total radioactivity, with a high loading (0.68), associated with CI15 and CI30 (loadings of 0.45 and 0.30, respectively). Relevant is the correlation between the γ-ray emission and the soil compaction, that could be explained with the frequent occurrence of Neapolitan Yellow Tuff (NYT) blocks in the subsurface soil. Indeed, the NYT is a high γ-ray emission source, due to its high content of K. The PC3 score map (Fig. 8c) shows a distribution pattern very similar to that observed for K and eTh, therefore can be assumed as representative of the natural variability of the surface soil mineralogy.

3.4. Environmental implications of the main findings

Often traditional soil sampling is not viable because of costs and labour requirements. Moreover, it needs a large number of soil samples

to achieve a good modelling and prediction of soil properties. This study has shown how proximal sensing technology and data analysis techniques may overcome the limitations of spatially scarce data. The proximal soil sensors used in this environmental context have the advantages to be non-invasive techniques, without any use of hazardous chemicals as well as time- and cost-efficient. In particular, geophysical methods proved to be a low cost and non-invasive way of collecting large amounts of information on various soil properties. The results of this study answered to the increasing demand of efficient, accurate, replicable over time but also cost effective and fast techniques for measuring soil properties related to land degradation factors, at a very fine spatial scale. The use of the pXRF spectrometer for analyzing PTEs concentration allowed to obtain a much larger number of non-invasive, no time-consuming and environmentally sustainable measures, overcoming the limitation of spatially scarce data frequently affecting the quality of prediction of the spatial models for the contaminant distribution. The relationship of the EMI sensor measured ECa data with the investigated PTEs (As, Pb and Sb) affecting the study area represented a further possibility to implement the spatial model with a low-cost technique able to acquire georeferenced data with higher density, improving spatial predictions. It is worthy of note that among the applied proximal sensors the EMI data were the better related to the PTEs, while the γ-ray data were the poorly related ones. That was somewhat expected as it is well known that covariates that are very useful for estimating properties related to soil genesis may not help much in the case of contaminants (Heuvelink and Webster, 2022). Particularly when there is a large number of measurements on soil samples as in this case study (174 soil samples at two soil depths in 38,500 m^2) and the quality of mapping soil contaminants is likely to depend largely on sample data.

An element of novelty and environmental relevance in our approach was the investigation by ultrasonic penetrometry that allowed to identify a large zone strongly affected by soil compaction in the most contaminated area. Soil compaction is among the processes leading to land degradation status since impairs soil functions and impedes root penetration and water, as well as gas exchange. It is frequently misunderstood and unconsidered in contaminated site surveys, despite so much affecting the soil-plant system and then of concern for future bioremediation plans of the site.

As general consideration, since the difficulty to know in advance what sensor will perform at the best, a multi-technique approach, as here proposed, represents a good compromise in the cost-benefit evaluation requested for the characterization plan by the law, also considering that frequently there is just a short period of time in which surveys are allowed due to administrative issues. Therefore, we are confident that the here tuned approach for the shooting range plant of Acerra could be efficiently exported in other sites affected by soil contamination.

4. Conclusions

A study was carried out to assess the degradation status of a field after being used for 10 years as an outdoor shooting range (OSR). The study was in Acerra (Naples, southern Italy) and based on a multisensor survey (electromagnetic induction, γ-ray spectrometry, ultrasonic penetrometry) coupled with laboratory measurements.

The electromagnetic induction (EMI) measurements allowed to reproduce the pattern of soil contamination due to the shooting activity. Indeed, the apparent electrical conductivity (ECa) data for the topsoil (ECa25) showed the highest values in the easternmost part of the field, in the direction (NNW-SSE) orthogonal to the shooting trajectories, where the highest contamination by PTEs (As, Pb, and Sb) measured by pXRF was found. Considering that the EMI data were the most densely measured and the most linearly correlated with As, Pb, and Sb, the ECa was used as covariate to improve the predictions of the measured PTEs, both within kriging with external drift and in the geostatistical turning bands simulation to assess their spatial uncertainty. Worthy of note, the maps of the spatial uncertainty showed no areas with particularly high values and that was probably due to the high sampling density.

Another proximal sensor that provided valuable results in this study was the ultrasonic penetrometer since it allowed to identify a large area strongly affected by soil compaction in the most contaminated field zone. Indeed, the soil compaction is frequently misunderstood and unconsidered in contaminated site surveys, despite it being among the processes leading to land degradation status. In this shooting field the soil compaction is very likely due to the transit of heavy vehicles for bullet fragments removal or to the development of plow pan under the lowest point of the tillage pass, when in the past the field was under crop cultivation. This soil issue is of concern and should be considered for future bioremediation plans of the site and soil health restoration. However, the cone index maps were consistent not only with the PTEs spatial distribution but also with the ECa pattern of the topsoil. Furthermore, the penetrometry survey and the core drillings data also allowed to identify the presence of yellow tuff blocks in the topsoil or near to the surface and their spatial variability was found consistent with the γ-ray maps. On the contrary, the γ-ray data did not show clear relationship neither with the ECa measures nor with the PTEs contamination and the shooting positions, revealing that the γ-ray spectrometry was not a useful technique for contamination variability assessment.

Other notable relationships among the proximal sensors measured variables and the laboratory analysis (i.e. PTEs and PAHs) were revealed by the multivariate statistical analysis performed with the robust method (rPCA). Indeed, the bottom soil ECa pattern (ECa180), which assumes irregular shape with no relation with the shooting trajectories, is found related with the soil thickness (frequently indicating the travertine layer depth in this site) and anticorrelated with the EMI measured magnetic susceptibility (MSa180). The consistency between the MSa values and presence of travertine layers near to the surface had already been partially confirmed by the core drillings and inferred by the steel rod surveys. Hence, considering that in such a geological context the assessment of the depth spatial variability of a travertine bench is relevant to evaluate possible risks for groundwater contamination, caused by the porous nature and the fractured state of the travertine, the EMI measures of deeper volumes (i.e., ECa180 and MSa180) revealed a good proxy for a preliminary identification of the underground stratigraphy. Results could be used for selecting areas of future monitoring activities on contaminants interaction with travertine/groundwater.

In conclusion, the maps obtained by the scores of the two first principal components (i.e., PC1 and PC2) synthesize, respectively, the anthropogenic effects produced by the shooting activities (including PAHs, Pb and Sb contamination, associated with soil compaction) and the close relationship between ECa and MSa with relevant stratigraphic layers of the bottom soil. Then, the PC1 map might suggest homogeneous zones within the shooting area that are suitable to be delineated and submitted in the future to precision remediation.

As a final remark, the simultaneous use of different proximal sensors and laboratory analysis is recommended for modelling the PTEs spatial distribution and identification of the most contaminated areas in sites affected by environmental concerns. The different proximal sensors measures are in some way complementary, and their concurrent application allows to better understand the environmental processes. Some of the sensed properties can help to model and map spatial variability of geochemical concentrations. In addition, it is advisable to always complement predicted maps with spatial uncertainty assessment. That to provide decision makers tools to develop suitable remediation plans.

Funding sources

This research was supported by PRIN 2017 (Progetti di Rilevante Interesse Nazionale)—2017BHH84R "Role of Soil-Plant-Microbial Interactions at Rhizosphere Level on the Biogeochemical Cycle and Fate of Contaminants in Agricultural Soils Under Phytoremediation with

Biomass Crops (RIZOBIOREM)."

CRediT authorship contribution statement

S. Vingiani: Writing – review & editing, Writing – original draft, Supervision, Resources, Methodology, Investigation, Funding acquisition, Conceptualization. **G. Buttafuoco:** Writing – review & editing, Writing – original draft, Visualization, Validation, Supervision, Resources, Methodology, Formal analysis. **M. Fagnano:** Resources, Project administration, Funding acquisition, Conceptualization. **A. Guarino:** Writing – original draft, Formal analysis, Data curation. **C. Perreca:** Visualization, Validation, Software, Formal analysis, Data curation. **S. Albanese:** Writing – review & editing, Writing – original draft, Supervision, Software, Methodology, Investigation, Formal analysis.

Declaration of competing interest

Massimo Fagnano, Stefano Albanese, Simona Vingiani reports financial support was provided by Italian Ministry of University and Research. If there are other authors, they declare that they have no known competing financial interests or personal relationships that could have appeared to influence the work reported in this paper.

Data availability

Data will be made available on request.

Acknowledgment

The authors thank the two anonymous reviewers of this paper for providing constructive comments, which have contributed to the improvement of the published version.

Appendix A. Supplementary data

Supplementary data to this article can be found online at https://doi.org/10.1016/j.scitotenv.2024.172398.

References

Agency for Toxic Substances and Disease Registry, 1992. Toxicological Profile for Antimony. U.S. Public Health Service, U.S. Department of Health and Human Services, Atlanta, GA.

Aitchison, J., 1986. The Statistical Analysis of Compositional Data, Journal of the Royal Statistical Society. Series B. Chapman and Hall, London - New York. https://doi.org/10.1007/978-94-009-4109-0.

Alloway, B.J., 2013. Sources of Heavy Metals and Metalloids in Soils. https://doi.org/10.1007/978-94-007-4470-7_2.

Altdorff, D., Bechtold, M., van der Kruk, J., Vereecken, H., Huisman, J.A., 2016. Mapping peat layer properties with multi-coil offset electromagnetic induction and laser scanning elevation data. Geoderma 261. https://doi.org/10.1016/j.geoderma.2015.07.015.

Andrade, R., Mancini, M., Teixeira, A.F., dos S Silva, S.H.G., Weindorf, D.C., Chakraborty, S., Guilherme, L.R.G., Curi, N., 2022. Proximal sensor data fusion and auxiliary information for tropical soil property prediction: soil texture. Geoderma 422. https://doi.org/10.1016/j.geoderma.2022.115936.

Armstrong, M., 1998. Basic Linear Geostatistics. Springer Berlin Heidelberg, Berlin, Heidelberg. https://doi.org/10.1007/978-3-642-58727-6.

ARPAV, 2014. Agenzia Regionale per la Prevenzione e Protezione Ambientale del Veneto. In: Proposte tecniche e legislative per la gestione di alcuni aspetti ambientali inerenti i poligoni di tiro, pp. 1–96.

Ayuso, R.A., De Vivo, B., Rolandi, G., Seal, R.R., Paone, A., 1998. Geochemical and isotopic (Nd–Pb–Sr–O) variations bearing on the genesis of volcanic rocks from Vesuvius, Italy. J. Volcanol. Geotherm. Res. 82, 53–78. https://doi.org/10.1016/S0377-0273(97)00057-7.

Barley, K.P., Farrell, D.A., Greacen, E.L., 1965. The influence of soil strength on the penetration of a loam by plant roots. Aust. J. Soil Res. 3 https://doi.org/10.1071/SR9650069.

Basunia, S., Landsberger, S., 2001. Contents and leachability of heavy metals (Pb, Cu, Sb, Zn, As) in soil at the pantex firing range, Amarillo, Texas. J. Air Waste Manage. Assoc. 51 https://doi.org/10.1080/10473289.2001.10464374.

Beamish, D., 2013. Gamma ray attenuation in the soils of Northern Ireland, with special reference to peat. J. Environ. Radioact. 115 https://doi.org/10.1016/j.jenvrad.2012.05.031.

Becker, R.A., Chambers, J.M., Wilks, A.R., 1988. The New S Language: A Programming Environment for Data Analysis and Graphics. Wadsworth and Brooks, Cole.

Ben-Dor, E., Taylor, R.G., Hill, J., Demattê, J.A.M., Whiting, M.L., Chabrillat, S., Sommer, S., 2008. Imaging spectrometry for soil applications. Adv. Agron. https://doi.org/10.1016/S0065-2113(07)00008-9.

Ben-Dor, E., Chabrillat, S., Demattê, J.A.M., Taylor, G.R., Hill, J., Whiting, M.L., Sommer, S., 2009. Using imaging spectroscopy to study soil properties. Remote Sens. Environ. 113, S38–S55. https://doi.org/10.1016/j.rse.2008.09.019.

Ben-Dor, E., Schläpfer, D., Plaza, A.J., Malthus, T., 2013. Hyperspectral remote sensing. In: Airborne Measurements for Environmental Research: Methods and Instruments. John Wiley & Sons, Ltd, pp. 413–456. https://doi.org/10.1002/9783527653218.ch8.

Binley, A., Cassiani, G., Deiana, R., 2010. Hydrogeophysics: opportunities and challenges. Boll. Geofis. Teor. Appl. 51.

Blanchar, R.W., Edmonds, C.R., Bradford, J.M., 1978. Root growth in cores formed from Fragipan and B2 horizons of Hobson soil. Soil Sci. Soc. Am. J. 42 https://doi.org/10.2136/sssaj1978.03615995004200030012x.

Bleines, C., Deraisme, J., Geffroy, F., Jeannée, N., Perseval, S., Rambert, F., 2023. Isatis.neo technical references (no. 2017.2). Geovariances. Avon Cedex 182.

Bouksila, F., Persson, M., Bahri, A., Berndtsson, R., 2012. Electromagnetic induction prediction of soil salinity and groundwater properties in a Tunisian Saharan oasis. Hydrol. Sci. J. 57 https://doi.org/10.1080/02626667.2012.717701.

Bowen, H.D., 1976. Correlation of penetrometer cone index with root impedance. In: Paper. American Society of Agricultural Engineers.

Busscher, W.S., Sojka, R.E., 1987. Enhancement of subsoiling effect on soil strength by conservation tillage. Transactions of the ASAE 30. https://doi.org/10.13031/2013.30493.

Buttafuoco, G., Quarto, R., Quarto, F., Conforti, M., Venezia, A., Vitti, C., Castrignanò, A., 2019. A geophysical and spectrometric sensor data fusion approach for homogeneous within-field zone delineation. In: Stafford, J.V. (Ed.), Precision Agriculture '19. Wageningen Academic Publishers, The Netherlands, pp. 705–712. https://doi.org/10.3920/978-90-8686-888-9_87.

Buttafuoco, G., Quarto, R., Quarto, F., Conforti, M., Venezia, A., Vitti, C., Castrignanò, A., 2021. Taking into account change of support when merging heterogeneous spatial data for field partition. Precis. Agric. 22, 586–607. https://doi.org/10.1007/s11119-020-09781-9.

Callegari, I., Bezzon, G. Pietro, Broggini, C., Buso, G.P., Caciolli, A., Carmignani, L., Colonna, T., Fiorentini, G., Guastaldi, E., Xhixha, M.K., Mantovani, F., Massa, G., Menegazzo, R., Mou, L., Pirro, A., Alvarez, C.R., Strati, V., Xhixha, G., Zanon, A., 2013. Total natural radioactivity, Tuscany. Italy. J Maps 9. https://doi.org/10.1080/17445647.2013.802999.

Cannatelli, C., 2012. Understanding magma evolution at Campi Flegrei (Campania, Italy) volcanic complex using melt inclusions and phase equilibria. Mineral. Petrol. 104 https://doi.org/10.1007/s00710-011-0182-6.

Cao, X., Ma, L.Q., Chen, M., Hardison, D.W., Harris, W.G., 2003. Weathering of Lead bullets and their environmental effects at outdoor shooting ranges. J. Environ. Qual. 32 https://doi.org/10.2134/jeq2003.5260.

Caporale, A.G., Adamo, P., Capozzi, F., Langella, G., Terribile, F., Vingiani, S., 2018a. Monitoring metal pollution in soils using portable-XRF and conventional laboratory-based techniques: evaluation of the performance and limitations according to metal properties and sources. Sci. Total Environ. 643 https://doi.org/10.1016/j.scitotenv.2018.06.178.

Caporale, A.G., Adamo, P., Capozzi, F., Langella, G., Terribile, F., Vingiani, S., 2018b. Monitoring metal pollution in soils using portable-XRF and conventional laboratory-based techniques: evaluation of the performance and limitations according to metal properties and sources. Sci. Total Environ. https://doi.org/10.1016/j.scitotenv.2018.06.178.

Carmichael, R.S., 2017. Practical handbook of physical properties of rocks and minerals (1988). Practical Handbook of Physical Properties of Rocks and Minerals 1988. https://doi.org/10.1201/9780203710968.

Carr, R., Zhang, C., Moles, N., Harder, M., 2008. Identification and mapping of heavy metal pollution in soils of a sports ground in Galway City, Ireland, using a portable XRF analyser and GIS. Environ. Geochem. Health. https://doi.org/10.1007/s10653-007-9106-0.

Cassiani, G., Binley, A., Kemna, A., Wehrer, M., Orozco, A.F., Deiana, R., Boaga, J., Rossi, M., Dietrich, P., Werban, U., Zschornack, L., Godio, A., JafarGandomi, A., Deidda, G.P., 2014. Noninvasive characterization of the Trecate (Italy) crude-oil contaminated site: links between contamination and geophysical signals. Environ. Sci. Pollut. Res. 21 https://doi.org/10.1007/s11356-014-2494-7.

Castrignanò, A., Buttafuoco, G., 2020. 3. Data processing. In: Castrignanò, A., Buttafuoco, G., Khosla, R., Mouazen, A., Moshou, D., Naud, O. (Eds.), Agricultural Internet of Things and Decision Support for Precision Smart Farming. Academic Press, London, UK, pp. 139–182. https://doi.org/10.1016/B978-0-12-818373-1.00003-2.

Castrignanò, A., Quarto, R., Venezia, A., Buttafuoco, G., 2019. A comparison between mixed support kriging and block cokriging for modelling and combining spatial data with different support. Precis. Agric. 20, 1–21. https://doi.org/10.1007/s11119-018-09630-w.

Censis Servizi, S. p. A, 2008. 1° RAPPORTO SPORT & SOCIETA.

César de Mello, D., Alexandre Melo Demattê, J., Alcantara de Oliveira Mello, F., Roberto Poppiel, R., ElizabetQuiñonez Silvero, N., Lucas Safanelli, J., Barros e Souza, A., Augusto Di Loreto Di Raimo, L., Rizzo, R., Eduarda Bispo Resende, M., Ernesto Gonçalves Reynaud Schaefer, C., 2021. Applied gamma-ray spectrometry for evaluating tropical soil processes and attributes. Geoderma 381, 114736. https://doi.org/10.1016/j.geoderma.2020.114736.

Chabrillat, S., Ben-Dor, E., Cierniewski, J., Gomez, C., Schmid, T., van Wesemael, B., 2019. Imaging spectroscopy for soil mapping and monitoring. Surv. Geophys. 40, 361–399. https://doi.org/10.1007/S10712-019-09524-0/TABLES/2.
Chen, M., Daroub, S.H., Ma, L.Q., Harris, W.G., Cao, X., 2002. Characterization of lead in soils of a rifle/pistol shooting range in Central Florida, USA. Soil Sediment Contam. 11 https://doi.org/10.1080/20025891106664.
Cheng, Q., Agterberg, F.P., Ballantyne, S.B., 1994. The separation of geochemical anomalies from background by fractal methods. J. Geochem. Explor. 51 https://doi.org/10.1016/0375-6742(94)90013-2.
Chilès, J.-P., Delfiner, P., 2012. Geostatistics: Modeling spatial uncertainty. In: Wiley Series in Probability and Statistics, 2nd Edition, 2nd ed. John Wiley & Sons, Inc., Hoboken, NJ, USA https://doi.org/10.1002/9781118136188.
Chiozzi, P., Pasquale, V., Verdoya, M., Minato, S., 2001. Natural gamma-radiation in the Aeolian volcanic arc. Appl. Radiat. Isot. 55 https://doi.org/10.1016/S0969-8043(01)00127-0.
Clausen, J., Korte, N., 2009. The distribution of metals in soils and pore water at three U. S. military training facilities. Soil Sediment Contam. 18 https://doi.org/10.1080/15320380903085683.
Climate Acerra by Climate-Data.org, 2024. Climate data [WWW Document]. https://it.climate-data.org/europa/italia/campania/acerra-14146/. https://it.climate-data.org/europa/italia/campania/acerra-14146/. accessed 3.26.24.
Comas-Cufí, M., Thió-Henestrosa, S., 2011. CoDaPack 2.0.
Conforti, M., Matteucci, G., Buttafuoco, G., 2018. Using laboratory Vis-NIR spectroscopy for monitoring some forest soil properties. J. Soils Sediments 18, 1009–1019. https://doi.org/10.1007/s11368-017-1766-5.
CONI, 2023. I numeri dello sport 2019–2020 [WWW Document]. Salone d'Onore del CONI Foro Italico Roma. URL. https://www.coni.it/it/i-numeri-dello-sport.html. accessed 9.15.23.
Cook, S.E., Corner, R.J., Groves, P.R., Grealish, G.J., 1996. Use of airborne gamma radiometric data for soil mapping. Aust. J. Soil Res. 34 https://doi.org/10.1071/SR9960183.
Corwin, D., 2005. Geospatial measurement of apparent soil electrical conductivity for characterizing soil spatial variability. In: Alvarez-Benedi, J., Munoz-Carpena, R. (Eds.), Soil-Water-Solute Process Characterization an Integrated Approach. CRC Press, Boca Raton, pp. 639–672. https://doi.org/10.1201/9781420032086.ch18.
Corwin, D.L., Lesch, S.M., 2005a. Characterizing soil spatial variability with apparent soil electrical conductivity: I. Survey protocols. Comput Electron Agric 46. https://doi.org/10.1016/j.compag.2004.11.002.
Corwin, D.L., Lesch, S.M., 2005b. Apparent soil electrical conductivity measurements in agriculture. Comput. Electron. Agric. 46 https://doi.org/10.1016/j.compag.2004.10.005.
Daniels, J.J., Ehsani, M.R., Allred, B.J., 2008a. Ground-penetrating radar methods (GPR). In: Allred, B.J., Daniels, J.J., Ehsani, M.R. (Eds.), Handbook of Agricultural Geophysics. CRC Press, Boca Raton, pp. 129–146.
Daniels, Jeffrey J., Vendl, M., Ehsani, M.R., Allred, B., 2008b. Electromagnetic induction methods. In: Allred, B., Daniels, J.J., Ehsani, M.R., Daniels, J.J., Ehsani, M.R. (Eds.), Handbook of Agricultural Geophysics. CRC Press, Boca Raton, pp. 109–128. https://doi.org/10.1201/9781420019353.
De Benedetto, D., Castrignano, A., Sollitto, D., Modugno, F., Buttafuoco, G., Papa, G.L.O., Lo, G.L.G., 2012. Integrating geophysical and geostatistical techniques to map the spatial variation of clay. Geoderma 171–172, 53–63. https://doi.org/10.1016/j.geoderma.2011.05.005.
De Vivo, B., Cicchella, D., Lima, A., Fortelli, A., Guarino, A., Zuzolo, D., Esposito, M., Cerino, R., Pizzolante, A., Albanese, S., 2021. Monitoraggio geochimico-ambientale dei suoli della regione Campania - Progetto Campania Trasparente. In: Elementi potenzialmente tossici e loro biodisponibilità, elementi maggiori e in traccia (distribuzione in suoli superficiali e profondi). Aracne Editrice, Roma, Volume 1. ISBN: 978-88-255-4036-9.
Deino, A.L., Orsi, G., de Vita, S., Piochi, M., 2004. The age of the Neapolitan Yellow Tuff caldera-forming eruption (Campi Flegrei caldera – Italy) assessed by 40Ar/39Ar dating method. J. Volcanol. Geotherm. Res. 133, 157–170. https://doi.org/10.1016/S0377-0273(03)00396-2.
Deutsch, C.V., Journel, A.G., 1997. GSLIB: Geostatistical Software Library and User's Guide, 2nd ed. Oxford University Press, New York.
Doolittle, J.A., Brevik, E.C., 2014. The use of electromagnetic induction techniques in soils studies. Geoderma 223–225, 33–45. https://doi.org/10.1016/J.GEODERMA.2014.01.027.
Duruoha, C., Piffer, C.R., Silva, P.A., 2007. Corn root length density and root diameter as affected by soil compaction and soil water content. IRRIGA 12. https://doi.org/10.15809/irriga.2007v12n1p14-26.
Egozcue, J.J., 2009. Reply to "On the Harker Variation Diagrams;..." by J.A. Cortés. Math. Geosci. https://doi.org/10.1007/s11004-009-9238-0.
Egozcue, J.J., Pawlowsky-Glahn, V., Mateu-Figueras, G., Barceló-Vidal, C., 2003. Isometric logratio transformations for compositional data analysis. Math. Geol. 35, 279–300. https://doi.org/10.1023/A:1023818214614.
Filella, M., Belzile, N., Chen, Y.W., 2002. Antimony in the environment: a review focused on natural waters I. Occurence. Earth Sci. Rev. 57 https://doi.org/10.1016/S0012-8252(01)00070-8.
Filzmoser, P., Hron, K., Reimann, C., 2009. Principal Component Analysis for Compositional Data with Outliers, in: Environmetrics. https://doi.org/10.1002/env.966.
di Gennaro, A., Terribile, F., 1999. I suoli della Provincia di Napoli. S.E.L.C.A, NAPOLI.
Gerard, C.J., Sexton, P., Shaw, G., 1982. Physical factors influencing soil strength and root growth 1. Agron. J. 74 https://doi.org/10.2134/agronj1982.00021962007400050025x.
Gholizadeh, A., Borùvka, L., Vašát, R., Saberioon, M., Klement, A., Kratina, J., Tejnecký, V., Drábek, O., 2015. Estimation of potentially toxic elements contamination in anthropogenic soils on a brown coal mining dumpsite by reflectance spectroscopy: a case study. PLoS One. https://doi.org/10.1371/journal.pone.0117457.
Gisbert, C., Ros, R., De Haro, A., Walker, D.J., Bernal, M.P., Serrano, R., Navarro-Aviñó, J., 2003. A plant genetically modified that accumulates Pb is especially promising for phytoremediation. Biochem. Biophys. Res. Commun. 303 https://doi.org/10.1016/S0006-291X(03)00349-8.
Goovaerts, Pierre, 1997. Geostatistics for Natural Resources Evaluation. Oxford University Press, New York, Applied Geostatistics Series.
Gotway Crawford, C.A., Young, L.J., 2005. Change of support: An inter-disciplinary challenge. In: Geostatistics for Environmental Applications. Springer, Berlin Heidelberg, Berlin, Heidelberg, pp. 1–13.
Gozukara, G., Zhang, Y., Hartemink, A.E., 2022. Using pXRF and Vis-NIR spectra for predicting properties of soils developed in loess. Pedosphere 32, 602–615. https://doi.org/10.1016/S1002-0160(21)60092-9.
Grasty, R.L., 1975. Atmospheric absorption of 2.62 Mev gamma-ray photons emitted from the ground. Geophysics 40. https://doi.org/10.1190/1.1440582.
Heil, K., Schmidhalter, U., 2017. The application of em38: determination of soil parameters, selection of soil sampling points and use in agriculture and archaeology. Sensors 17, 2540. https://doi.org/10.3390/s17112540.
Heuvelink, G.B.M., Webster, R., 2022. Spatial statistics and soil mapping: a blossoming partnership under pressure. Spat Stat 50, 100639. https://doi.org/10.1016/j.spasta.2022.100639.
Higueras, P., Oyarzun, R., Iraizoz, J.M., Lorenzo, S., Esbrí, J.M., Martínez-Coronado, A., 2012. Low-cost geochemical surveys for environmental studies in developing countries: testing a field portable XRF instrument under quasi-realistic conditions. J. Geochem. Explor. https://doi.org/10.1016/j.gexplo.2011.02.005.
Horta, A., Malone, B., Stockmann, U., Minasny, B., Bishop, T.F.A., McBratney, A.B., Pallasser, R., Pozza, L., 2015. Potential of integrated field spectroscopy and spatial analysis for enhanced assessment of soil contamination: a prospective review. Geoderma. https://doi.org/10.1016/j.geoderma.2014.11.024.
Hou, X., He, Y., Jones, B.T., 2004. Recent advances in portable x-ray fluorescence spectrometry. Appl. Spectrosc. Rev. https://doi.org/10.1081/ASR-120028867.
Houben, J.M., 1974. Root development and soil conditions. Bedrijfsontwikkeling, 5, pp. 141–148.
Hron, K., Filzmoser, P., 2015. Exploring compositional data with the robust compositional biplot, in: studies in theoretical and applied statistics. Selected Papers of the Statistical Societies. https://doi.org/10.1007/10104_2014_1.
Huang, J., Lark, R.M., Robinson, D.A., Lebron, I., Keith, A.M., Rawlins, B., Tye, A., Kuras, O., Raines, M., Triantafilis, J., 2014. Scope to predict soil properties at within-field scale from small samples using proximally sensed γ-ray spectrometer and EM induction data. Geoderma 232–234. https://doi.org/10.1016/j.geoderma.2014.04.031.
I.G.M. Istituto Geografico Militare, 1967. Foglio Geologico Napoli, 183–184 [WWW Document]. URL. http://sgi.isprambiente.it/geologia100k/mostra_foglio.aspx?numero_foglio=183-184.
IAEA (International Atomic Energy Agency), 2004. Soil Sampling for Environmental Contaminants. Austria.
Ishtiaq, M., Jehan, N., Khan, S.A., Muhammad, S., Saddique, U., Iftikhar, B., Zahidullah, 2018. Potential harmful elements in coal dust and human health risk assessment near the mining areas in Cherat. Pakistan. Environmental Science and Pollution Research 25. https://doi.org/10.1007/s11356-018-1655-5.
ITRC (Interstate Technology and Regulatory Council Small Arms Firing Range Team), 2003. Characterization and Remediation of Soils at Closed Small Arms Firing Ranges.
IUSS Working Group WRB, 2014. World reference base for soil resources 2014. International soil classification system for naming soils and creating legends for soil maps, World Soil Resources Reports No. 106 https://doi.org/10.1017/S0014797706394902.
Johnson, C.A., Moench, H., Wersin, P., Kugler, P., Wenger, C., 2005. Solubility of antimony and other elements in samples taken from shooting ranges. J. Environ. Qual. 34 https://doi.org/10.2134/jeq2005.0248.
Jones, M.C., Aitchison, J., 1987. The statistical analysis of compositional data. J. R. Stat. Soc. Ser. A 150. https://doi.org/10.2307/2982045.
Journel, A.G., 1983. Nonparametric estimation of spatial distributions. J. Int. Assoc. Math. Geol. 15, 445–468. https://doi.org/10.1007/BF01031292.
Kees, G., 2005. Hand-Held Electronic Cone Penetrometers for Measuring Soil Strength. 2E22E60—Soil Strength Tester 2600.
Knox .A.D.C.,.P.G., A.S.S.J., 2000. Chemophytostabilization of metals in contaminated soils. In: Wise, D.L., Trantolo, D.J., Cichon, E.J., Inyang, H.I., Stottmeister, U. (Eds.), Bioremediation of Contaminated Soils. Marcel Dekker, Inc., New York, pp. 811–836.
Kweon, G., Lund, E., Maxton, C., 2013. Soil organic matter and cation-exchange capacity sensing with on-the-go electrical conductivity and optical sensors. Geoderma 199. https://doi.org/10.1016/j.geoderma.2012.11.001.
Kynčlová, P., Filzmoser, P., Hron, K., 2016. Compositional biplots including external non-compositional variables. Statistics (Ber) 50. https://doi.org/10.1080/02331888.2015.1135155.
Lagacherie, P., Gomez, C., 2018. Vis-NIR-SWIR Remote Sensing Products as New Soil Data for Digital Soil Mapping, pp. 415–437. https://doi.org/10.1007/978-3-319-63439-5_13.
Lantuéjoul, C., 2002. Geostatistical simulation. Springer Berlin Heidelberg, Berlin, Heidelberg. https://doi.org/10.1007/978-3-662-04808-5.
Laporte-Saumure, M., Martel, R., Mercier, G., 2011. Characterization and metal availability of copper, lead, antimony and zinc contamination at four Canadian small

arms firing ranges. Environ. Technol. 32 https://doi.org/10.1080/09593330.2010.512298.
Law Decree 152, 2006. Norme in Materia Ambientale. Part IV. Title V., Gazzetta Ufficiale della Repubblica Italiana. Rome, Italy.
Leuangthong, O., McLennan, J.A., Deutsch, C.V., 2004. Minimum acceptance criteria for geostatistical realizations. Nat. Resour. Res. 13, 131–141. https://doi.org/10.1023/B:NARR.0000046916.91703.bb.
Lima, A., De Vivo, B., Fedele, L., Sintoni, F., Milia, A., 2007. Geochemical variations between the 79 AD and 1944 AD Somma–Vesuvius volcanic products: constraints on the evolution of the hydrothermal system based on fluid and melt inclusions. Chem. Geol. 237, 401–417. https://doi.org/10.1016/j.chemgeo.2006.07.011.
Loonstra, E.H., 2011. Gamma and electro magnetics: a multi-sensor approach for the mapping of water related soil properties. In: Proceeding of the Second Global Workshop on Proximal Soil Sensing. Montreal.
Martelet, G., Drufin, S., Tourliere, B., Saby, N.P.A., Perrin, J., Deparis, J., Prognon, F., Jolivet, C., Ratié, C., Arrouays, D., 2013. Regional regolith parameter prediction using the proxy of airborne gamma ray spectrometry. Vadose Zone J. 12 https://doi.org/10.2136/vzj2013.01.0003.
Martínez, G., Vanderlinden, K., Giráldez, J.V., Espejo, A.J., Muriel, J.L., 2010. Field-scale soil moisture pattern mapping using electromagnetic induction. Vadose Zone J. 9 https://doi.org/10.2136/vzj2009.0160.
Martini, E., Werban, U., Zacharias, S., Pohle, M., Dietrich, P., Wollschläger, U., 2017. Repeated electromagnetic induction measurements for mapping soil moisture at the field scale: validation with data from a wireless soil moisture monitoring network. Hydrol. Earth Syst. Sci. 21 https://doi.org/10.5194/hess-21-495-2017.
Matheron, G., 1963. Principles of geostatistics. Econ. Geol. 58, 1246–1266. https://doi.org/10.2113/gsecongeo.58.8.1246.
Matheron, G., 1971. The Theory of Regionalized Variables and its Applications, Les Cahiers du Centre de Morphlogie Mathematique. Ecole Nationale Superieure des Mines de Paris, Fontainebleau.
Matheron, G., 1973. The intrinsic random functions and their applications. Adv. Appl. Probab. 5, 439–468. https://doi.org/10.2307/1425829.
McBratney, A.B., Minasny, B., Whelan, B.M., 2005. Obtaining 'useful' high-resolution soil data from proximally-sensed electrical conductivity/resistivity (PSEC/R) surveys., in: proceedings of the 5th European conference on precision agriculture. Wageningen Academic Publishers, The Netherlands, pp. 503–510.
McBratney, A.B., Minasny, B., Whelan, B., 2011. Defining proximal soil sensing. In: Adamchuk, V.I., Viscarra Rossel, R.A. (Eds.), The Second Global Workshop on Proximal Soil Sensing. McGill University, Montreal, pp. 144–146.
Mileti, F.A., Langella, G., Prins, M.A., Vingiani, S., Terribile, F., 2013. The hidden nature of parent material in soils of Italian mountain ecosystems. Geoderma 207–208. https://doi.org/10.1016/j.geoderma.2013.05.006.
Ministry Decree n. 46, 2019. Gazzetta Ufficiale della Repubblica, Anno 160°, n. 132.
Molin, J.P., Faulin, G.D.C., 2013. Spatial and temporal variability of soil electrical conductivity related to soil moisture. Sci. Agric. 70 https://doi.org/10.1590/s0103-90162013000100001.
Muhammad, S., Ullah, R., Jadoon, I.A.K., 2019. Heavy metals contamination in soil and food and their evaluation for risk assessment in the Zhob and Loralai valleys, Baluchistan province, Pakistan. Microchem. J. 149 https://doi.org/10.1016/j.microc.2019.103971.
Mullins, C.E., 1977. Magnetic susceptibility of the soil and its significance in soil science - a review. J. Soil Sci. 28, 223–246. https://doi.org/10.1111/j.1365-2389.1977.tb02232.x.
Nanzyo, M., 2002. Unique properties of volcanic ash soils. Global. J. Environ. Res. 6.
Noll, M., 2003. Trace elements in terrestrial environments: biogeochemistry, bioavailability, and risks of metals, 2nd edition. J. Environ. Qual. 32.
Olea, R.A., 1999. Geostatistics for Engineers and Earth Scientists, Geostatistics for Engineers and Earth Scientists. Springer US, New York. https://doi.org/10.1007/978-1-4615-5001-3.
Padarian, J., McBratney, A.B., 2023. QuadMap: variable resolution maps to better represent spatial uncertainty. Comput. Geosci. 181, 105480 https://doi.org/10.1016/j.cageo.2023.105480.
Pawlowsky-Glahn, V., Buccianti, A., 2011. Compositional Data Analysis: Theory and Methods.
Pawlowsky-Glahn, V., Egozcue, J.J., Tolosana-Delgado, R., 2015. Modelling and Analysis of Compositional Data. Statistics in practice. John Wiley & Sons, Ltd, Chichester, UK.
Paz, A.M., Castanheira, N., Farzamian, M., Paz, M.C., Gonçalves, M.C., Monteiro Santos, F.A., Triantafilis, J., 2020. Prediction of soil salinity and sodicity using electromagnetic conductivity imaging. Geoderma 361, 114086. https://doi.org/10.1016/J.GEODERMA.2019.114086.
Pearson, K., 1896. VII. Mathematical contributions to the theory of evolution.-III. Regression, heredity, and panmixia. Phil. Trans. R. Soc. A 187, 253–318. https://doi.org/10.1098/rsta.1896.0007.
Priori, S., Bianconi, N., Costantini, E.A.C., 2014. Can γ-radiometrics predict soil textural data and stoniness in different parent materials? A comparison of two machine-learning methods. Geoderma 226–227. https://doi.org/10.1016/j.geoderma.2014.03.012.
Provincia di Napoli, 1998. Carta Tecnica Numerica Derivata - Sez. 448010 - Montefibre.
Putignano, M.L., Orrù, P.E., Schiattarella, M., 2012. Palaeoenvironmental Reconstruction of Holocene Coastline of Procida Island, Bay of Naples, in: Rendiconti Online Societa Geologica Italiana.
Randich, E., Duerfeldt, W., McLendon, W., Tobin, W., 2002. A metallurgical review of the interpretation of bullet lead compositional analysis. Forensic Sci. Int. 127 https://doi.org/10.1016/S0379-0738(02)00118-4.
Reynolds, J.M., 1997. An introduction to applied and environmental geophysics, An introduction to applied and environmental geophysics. https://doi.org/10.1071/pvv2011n155other.
Rhoades, J.D., Shouse, P.J., Alves, W.J., Manteghi, N.A., Lesch, S.M., 1990. Determining soil salinity from soil electrical conductivity using different models and estimates. Soil Sci. Soc. Am. J. 54 https://doi.org/10.2136/sssaj1990.03615995005400010007x.
Ribeiro, B.T., Silva, S.H.G., Silva, E.A., 2017. Portable X-ray fluorescence (pXRF) applications in tropical soil science. Cienc. Agrotecnol. 41, 245–254. https://doi.org/10.1590/1413-70542017413000117.
Rooney, C.P., Mclaren, R.G., Cresswell, R.J., 1999. Distribution and phytoavailability of lead in a soil contaminated with lead shot. Water Air Soil Pollut. 116 https://doi.org/10.1023/A:1005181303843.
Rosolem, C.A., Assis, J.S., Santiago, A.D., 1994. Root growth and mineral nutrition of corn hybrids as affected by phosphorus and lime. Commun. Soil Sci. Plant Anal. 25 https://doi.org/10.1080/00103629409369202.
Sadatcharam, K., Altdorff, D., Unc, A., Krishnapillai, M., Galagedara, L., 2020. Depth sensitivity of apparent magnetic susceptibility measurements using multi-coil and multi-frequency electromagnetic induction. J. Environ. Eng. Geophys. 25 https://doi.org/10.32389/JEEG20-001.
Saddique, U., Muhammad, S., Tariq, M., Zhang, H., Arif, M., Jadoon, I.A.K., Khattak, N. U., 2018. Potentially toxic elements in soil of the Khyber Pakhtunkhwa province and tribal areas, Pakistan: evaluation for human and ecological risk assessment. Environ. Geochem. Health 40. https://doi.org/10.1007/s10653-018-0091-2.
Sadeghi, B., 2023. Concentration-Area Plot. https://doi.org/10.1007/978-3-030-85040-1_64.
Saey, T., Note, N., Gheyle, W., Stichelbaut, B., Bourgeois, J., Van Eetvelde, V., Van Meirvenne, M., 2016. EMI as a non-invasive survey technique to account for the interaction between WW I relicts and the soil environment at the Western front. Geoderma. https://doi.org/10.1016/j.geoderma.2015.11.020.
Scheetz, C.D., Rimstidt, J.D., 2009. Dissolution, transport, and fate of lead on a shooting range in the Jefferson National Forest near Blacksburg, VA, USA. Environ. Geol. 58 https://doi.org/10.1007/s00254-008-1540-5.
Schuler, U., Erbe, P., Zarei, M., Rangubpit, W., Surinkum, A., Stahr, K., Herrmann, L., 2011. A gamma-ray spectrometry approach to field separation of illuviation-type WRB reference soil groups in northern Thailand. J. Plant Nutr. Soil Sci. 174 https://doi.org/10.1002/jpln.200800323.
Singh, B., Gräfe, M., 2010. Synchrotron-Based Techniques in Soils and Sediments, 1st ed. Developments in Soil Science, Elsevier, Burlington, MA.
Soil Survey Staff - NRCS/USDA, 2014. Keys to soil taxonomy. Soil Conservation Service 12.
Stelluti, M., Maiorana, M., De Giorgio, D., 1998. Multivariate approach to evaluate the penetrometer resistance in different tillage systems. Soil Tillage Res. 46 https://doi.org/10.1016/S0167-1987(98)00028-2.
Stevens, A., van Wesemael, B., Bartholomeus, H., Rosillon, D., Tychon, B., Ben-Dor, E., 2008. Laboratory, field and airborne spectroscopy for monitoring organic carbon content in agricultural soils. Geoderma 144, 395–404. https://doi.org/10.1016/j.geoderma.2007.12.009.
Taylor, H.M., 1973. Effects of soil strength on seedling emergence, root growth and crop yield. J. Terrramech. 9 https://doi.org/10.1016/0022-4898(73)90178-x.
Taylor, H.M., Ratliff, L.F., 1969. Root elongation rates of cotton and peanuts as a function of soil strength and soil water content. Soil Sci. 108 https://doi.org/10.1097/00010694-196908000-00006.
Taylor, H.M., Roberson, G.M., Parker, J.J., 1966. Soil strength-root penetration relations for medium- to coarse-textured soil materials. Soil Sci. 102 https://doi.org/10.1097/00010694-196607000-00002.
Taylor, J.A., Short, M., McBratney, A.B., Wilson, J., 2010. Comparing the ability of multiple soil sensors to predict soil properties in a Scottish potato production system. In: Viscarra Rossel, R.A., McBratney, A.B., Minasny, B. (Eds.), Proximal Soil Sensing, pp. 387–396.
Teixeira, A.F. dos S., Andrade, R., Mancini, M., Silva, S.H.G., Weindorf, D.C., Chakraborty, S., Guilherme, L.R.G., Curi, N., 2022. Proximal sensor data fusion for tropical soil property prediction: soil fertility properties. J. S. Am. Earth Sci. 116, 103873 https://doi.org/10.1016/j.jsames.2022.103873.
Templ, M., Hron, K., Filzmoser, P., 2011. robCompositions: An R-package for Robust Statistical Analysis of Compositional Data, in: Compositional Data Analysis: Theory and Applications. https://doi.org/10.1002/9781119976462.ch25.
Tite, M., Mullins, C., 1969. Electromagnetic prospecting: a preliminary investigation. Prospezioni Archeologiche 4, 95–102.
Tolosana-Delgado, R., Mueller, U., 2021. Geostatistics for compositional data with R, use R! Springer International Publishing, Cham. https://doi.org/10.1007/978-3-030-82568-3.
Tolosana-Delgado, R., Mueller, U., van den Boogaart, K.G., 2019. Geostatistics for compositional data: an overview. Math. Geosci. 51, 485–526. https://doi.org/10.1007/s11004-018-9769-3.
Triantafilis, J., Lesch, S.M., La Lau, K., Buchanan, S.M., 2009. Field level digital soil mapping of cation exchange capacity using electromagnetic induction and a hierarchical spatial regression model. Aust. J. Soil Res. 47 https://doi.org/10.1071/SR08240.
Trouse, A.C., 1983. Observations on under-the-row subsoiling after conventional tillage. Soil Tillage Res. 3 https://doi.org/10.1016/0167-1987(83)90018-1.
U.S. Army Corps of Engineers Fort Worth District, F.W.T, 2014. Remedial Investigation/Feasibility Study for the U.S. Border Patrol Firing Range. U.S. Customs and Border Protection. (Contract Number: W9126G-06-D-0016. Task Order 0039).
US EPA, 1979. Water Related Fate of the 129 Priority Pollutants, vol. 1. USEPA, Washington, DC.

US EPA, 2001. BBest Management Practices for Lead at Outdoor Shooting Range Outdoor Shooting Ranges.
U.S. EPA, 2014. Method 8270E (SW-846): Semivolatile Organic Compounds by Gas Chromatography/Mass Spectrometry (GC/MS). Washington, DC.
Van Der Klooster, E., Van Egmond, F.M., Sonneveld, M.P.W., 2011a. Mapping soil clay contents in Dutch marine districts using gamma-ray spectrometry. Eur. J. Soil Sci. 62, 743–753. https://doi.org/10.1111/j.1365-2389.2011.01381.x.
Van Der Klooster, E., Van Egmond, F.M., Sonneveld, M.P.W., 2011b. Mapping soil clay contents in Dutch marine districts using gamma-ray spectrometry. Eur. J. Soil Sci. 62 https://doi.org/10.1111/j.1365-2389.2011.01381.x.
Van Groenigen, J.W., Mutters, C.S., Horwath, W.R., Van Kessel, C., 2003. NIR and DRIFT-MIR spectrometry of soils for predicting soil and crop parameters in a flooded field. Plant Soil 250, 155–165. https://doi.org/10.1023/A:1022893520315.
Vingiani, S., Scarciglia, F., Mileti, F.A., Donato, P., Terribile, F., 2014. Occurrence and origin of soils with andic properties in Calabria (southern Italy). Geoderma 232–234. https://doi.org/10.1016/j.geoderma.2014.06.001.
Vingiani, S., Buonanno, M., Coraggio, S., D'Antonio, A., De Mascellis, R., Di Gennaro, A., Iamarino, M., Langella, G., Manna, P., Moretti, P., Terribile, F., 2018. Soils of the aversa plain (Southern Italy). J. Maps 14. https://doi.org/10.1080/17445647.2018.1458338.
Vingiani, S., Agrillo, A., De Mascellis, R., Langella, G., Manna, P., Mileti, F.A., Terribile, F., 2022. Multi-sensor approach combined with pedological investigations to understand site-specific variability of soil properties and potentially toxic elements (PTEs) content of an industrial contaminated area. Applied Sciences (Switzerland) 12. https://doi.org/10.3390/app12083993.
Viscarra Rossel, R.A., Taylor, H.J., McBratney, A.B., 2007. Multivariate calibration of hyperspectral γ-ray energy spectra for proximal soil sensing. Eur. J. Soil Sci. 58 https://doi.org/10.1111/j.1365-2389.2006.00859.x.
Viscarra Rossel, R.A., Adamchuk, V.I., Sudduth, K.A., McKenzie, N.J., Lobsey, C., 2011. Proximal soil sensing. An effective approach for soil measurements in space and time. Adv. Agron. 113, 237–282. https://doi.org/10.1016/B978-0-12-386473-4.00010-5.
Voorhees, W.B., 1987. Assessment of soil susceptibility to compaction using soil and climatic data bases. Soil Tillage Res. 10 https://doi.org/10.1016/0167-1987(87)90005-5.
Wackernagel, Hans, 2003. Multivariate Geostatistics : An Introduction with Applications. Springer.
Walter, J., Lück, E., Bauriegel, A., Richter, C., Zeitz, J., 2015. Multi-scale analysis of electrical conductivity of peatlands for the assessment of peat properties. Eur. J. Soil Sci. 66 https://doi.org/10.1111/ejss.12251.
Wang, D., Chakraborty, S., Weindorf, D.C., Li, B., Sharma, A., Paul, S., Ali, M.N., 2015. Synthesized use of VisNIR DRS and PXRF for soil characterization: Total carbon and total nitrogen. Geoderma. https://doi.org/10.1016/j.geoderma.2014.12.011.
Webster, R., Oliver, M.A., 2007. Geostatistics for Environmental Scientists, Statistics in Practice. John Wiley & Sons, Ltd, Chichester, UK. https://doi.org/10.1002/9780470517277.
Weindorf, D.C., Bakr, N., Zhu, Y., 2014. Advances in Portable X-ray Fluorescence (PXRF) for Environmental, Pedological, and Agronomic Applications, pp. 1–45. https://doi.org/10.1016/B978-0-12-802139-2.00001-9.
Wong, M.T.F., Harper, R.J., 1999. Use of on-ground gamma-ray spectrometry to measure plant-available potassium and other topsoil attributes. Aust. J. Soil Res. 37 https://doi.org/10.1071/S98038.
Wong, M.T.F., Asseng, S., Robertson, M.J., Oliver, Y., 2008. Mapping Subsoil Acidity and Shallow Soil across a Field with Information from Yield Maps, Geophysical Sensing and the Grower, in: Precision Agriculture. https://doi.org/10.1007/s11119-008-9052-6.
Wong, M.T.F., Oliver, Y.M., Robertson, M.J., 2009. Gamma-radiometric assessment of soil depth across a landscape not measurable using electromagnetic surveys. Soil Sci. Soc. Am. J. 73 https://doi.org/10.2136/sssaj2007.0429.
Wong, M.T.F., Wittwer, K., Oliver, Y.M., Robertson, M.J., 2010. Use of EM38 and Gamma Ray Spectrometry as Complementary Sensors for High-Resolution Soil Property Mapping, in: Proximal Soil Sensing. https://doi.org/10.1007/978-90-481-8859-8_29.
Zerboni, A., Trombino, L., Cremaschi, M., 2011. Micromorphological approach to polycyclic pedogenesis on the Messak Settafet plateau (Central Sahara): formative processes and palaeoenvironmental significance. Geomorphology 125, 319–335. https://doi.org/10.1016/j.geomorph.2010.10.015.